Guiding Epilepsy Surgery by Intraoperatively Visualizing Proinflammatory Microglia via a Ratiometric Surface-Enhanced Raman Scattering Nanosensor

Cong Wang[1,2,3,&], Zhi Li[4,&], Xiao Zhu[5], Yue Ding[6], Wenjia Duan[1], Wanbing Sun[7], Yiqing Jiang[1], Ming Chen[4], Jiayi Hu[1], Zheping Cai[8,9], Jing Zhao[1], Zhen Fan[4], Faming Zheng[10], Xingyu Zhou[11] Fang Xie[12], Jianping Zhang[13], Yihui Guan[12], Xiao Xiao[8,9,*], Liang Chen[4,9,14,15,*], Cong Li[1,*] and Ying Mao[4,9,14,*]

1. Key Laboratory of Smart Drug Delivery, Ministry of Education, State Key Laboratory of Medical Neurobiology, School of Pharmacy, Fudan University, Shanghai, China.
2. Academy for Engineering and Technology, Fudan University, Shanghai, China.
3. Shanghai Center for Brain Science and Brain-Inspired Technology, Shanghai, China.
4. Department of Neurosurgery, Huashan Hospital, Fudan University, Shanghai, China.
5. Department of Clinical Pharmacy and Pharmacy Administration, School of Pharmacy, Fudan University, 201203, China
6. Shanghai Mental Health Center, Shanghai Jiao Tong University School of Medicine, Shanghai, China.
7. Department of Neurology and Research Center of Neurology in Second Affiliated Hospital and Key Laboratory of Medical Neurobiology of Zhejiang Province, Zhejiang University School of Medicine, Hangzhou, China.
8. Key Laboratory of Computational Neuroscience and Brain-Inspired Intelligence, Ministry of Education; Behavioral and Cognitive Neuroscience Center, Institute of Science and Technology for Brain-Inspired Intelligence, Shanghai, China.
9. State Key Laboratory of Medical Neurobiology and MOE Frontiers Center for Brain Science, Shanghai, China.
10. State Key Laboratory of Transducer Technology, Shanghai Institute of Microsystem and Information Technology, Chinese Academy of Sciences, Shanghai, China.
11. Biomedical Engineering, Vanderbilt University, Nashville TN, USA.
12. PET Center, Huashan Hospital, Fudan University, Shanghai, China.
13. Shanghai Engineering Research Center for Molecular Imaging Probes, Shanghai, China.
14. National Center for Neurological Disorders, Shanghai, China.
15. Tianqiao and Chrissy Chen Institute for Translational Research, Shanghai, China.

[&]These authors contributed equally

*Corresponding authors, maoying@fudan.edu.cn; congli@fudan.edu.cn; hschenliang@fudan.edu.cn; xiaoxiao@fudan.edu.cn

Materials. Analytical grade solvents including methanol (CH_3OH), dichloromethane (CH_2Cl_2), and ether were purchased from Sinopharm Chemical Reagent. Anhydrous CH_2Cl_2 and anhydrous N,N′-dicyclohexylcarbodiimide (DMF) were purchased from Titan Scientific. Salicylhydroxamic acid (SHA) and kainic-acid (KA), were purchased from Sigma-Aldrich. A Bruker AC400 or a Bruker AC600 NMR (Bruker Daltonics, MA) was used for recording spectrometer ^{1}H NMR and ^{13}C NMR spectra. Chemical shifts of compounds were referenced to residue solvent peaks or tetramethylsilane as the internal reference and given in ppm. Electrospray ionization-high resolution mass spectra (ESI-HRMS) were obtained on an AB SCIEX TRIPLE TOF 5600+ mass spectrometer (AB Sciex, CA). Amino polyethylene glycol maleimide (NH_2-PEG-Mal, Mw ≈ 5000) was provided by Shanghai Ponsure Biotech, Inc. Thiolated polyethylene glycol (SH-PEG, Mw ≈ 5000) was purchased from Beijing Jenkem Technology Company. The cysteine-modified angiopep2 peptide (TFFYGGSRGKRNNFKTEEYC, Mw = 2404.6) was purchased from Chinese Peptide Company. Fluoro-Jade B (Fjb), an anionic fluorescein derivative for staining degenerating neurons, was purchased from Chemicon International. The bicinchoninic acid (BCA) protein assay kit, 2-(4-amidinophenyl)-6-indolecarbamidine dihydrochloride (DAPI), immune staining blocking buffer, intracellular staining perm wash buffer, fixation buffer, RIPA buffer and QuickBlock blocking buffer were purchased from Beyotime. The SYBR Premix Ex Taq Kit and PrimeScript™ RT Master Mix were purchased from TAKARA Bio. A Tissue RNA Purification Kit was obtained from EZBioscience. Bovine serum albumin was purchased from Solarbio Life Sciences. Super electrochemiluminescence (ECL) detection Reagent was obtained from Yeasen Biotechnology (Shanghai) Co., Ltd. Amplite™ fluorimetric hypochlorite (hypochlorous acid) assay kit was purchased from AAT Bioquest. Cell Counting Kit-8 (CCK-8) assay was obtained from Meilunbio®. Radioactive tracers ^{18}F-DPA714 and ^{18}F-FDG were obtained from Huashan Hospital PET Center and Shanghai Cancer Center, respectively. Ultrapure water (a specific resistance of 18.2 $M\Omega\cdot cm^{-1}$) was used throughout the study.

Immunoblotting. After harvesting brain tissues or cultured cells, we lysed them with RIPA buffer with a 1% protease inhibitor cocktail. The tissues were homogenized using a tissue grinder (MX-2018, Jinxin, China) (90 Hz, 60 s). The lysed samples were centrifuged (14,000 g, 4 °C, 20 min). After determining protein concentrations with a BCA assay, we mixed the supernatants with loading buffer (5×), boiled (95 °C, 10 min), followed by cooling (0 °C, 3 min). The proteins were separated by 10% SDS PAGE and transformed to a nitrocellulose membrane in an ice bath. The membranes were blocked with 5% skimmed milk in triethanolamine buffered saline-tween (TBS-T) at r.t. for 1 h. Then we incubated the membranes with primary antibodies overnight at 4 °C (Supplementary Table 4), followed with HRP-conjugated secondary antibodies (1:10000, YEASEN) at r.t. for 2 h. The immunoblot images were visualized on ChemiDocTM MP Imaging System (Bio-Rad, Hercules, CA), and cumulative densitometric analyses were performed with Image J (Version 1.53k).

Flow cytometric analysis. For cultured cellular studies, cellular suspensions were harvested and centrifuged (2,800 g, 3 min) at 4 °C. For cell-surface marker staining, we blocked the cells with 5% BSA-PBS at r.t. for 10 min. For intracellular marker staining, the cells were permeated first, and then blocked as described above. After staining with fluorophore-conjugated primary antibodies (Supplementary Table 4) at r.t. for 20 min, the cells were fixed with fixation buffer, washed and resuspended with PBS. For tissue-based analysis, the brain tissues were collected from patients or mice, minced with scissors, and mechanically homogenated in Cell Staining Buffer (Biolegend, Cat# 420201). Single-cell suspensions were obtained by filtering with a 70-μm membrane filter. The following procedure and antibodies used were identical to the *in vitro* flow cytometry for cells described above. Flow cytometric data were collected on a BD LSR flow cytometer (Becton, Dickinson and Company, Maryland) and analyzed using FlowJo software (Version 10.4.2).

Determination of hypochlorite concentration *in vitro*. For *ex vivo* HOCl measurement, fresh brain tissues were harvested and homogenized in ice-cold PBS (pH 7.4) with a ratio of 1:7 volumes (W/V) by using a tissue grinder (60 Hz, 120 s). The above solutions were ultrasound for 10 min and then centrifuged (10,000 g, 4 °C, 10 min). For cellular HOCl measurement, the harvested microglia with different phenotypes were lysed with RIPA buffer and centrifuged (10,000 g, 4 °C, 10 min). We collected the homogenate supernatants for the following tests according to the supplier’s instructions. We calculated the HOCl concentration according to a calibration curve.

Synthetic route of Lip-Cy7S

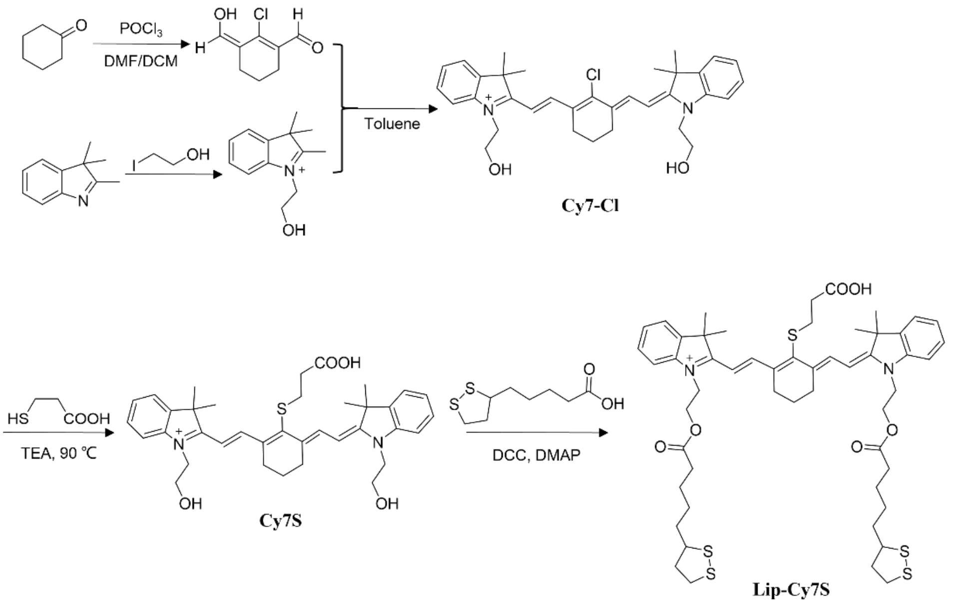

Supplementary Scheme 1 | Synthesis of Lip-Cy7S.

Cy7S. The Cy7Cl was synthesized according to our previous publication[1]. Then the reaction material Cy7Cl (109 mg, 0.2 mmol), 3-mercaptopropionic acid (25 mg, 0.24 mmol) and triethylamine (TEA, 30 mg, 0.3 mmol) were dissolved in anhydrous DMF and stirred at r.t. for 24 h. Then the product was recrystallized in ether and obtained as green precipitate after filtrating. The solid was purified via silica gel chromatography with the gradient of CH_2Cl_2/CH_3OH (from 50: 1 to 5: 1) to afford Cy7S as a green powder. Yield: 169.3 mg (75%). ^1H NMR (400 MHz, Methanol-d_4): δ 8.90 (d, J = 14.2 Hz, 2H), 7.49 (dd, J = 7.6, 3.9 Hz, 1H), 7.43 – 7.35 (m, 2H), 7.31 (dd, J = 8.3, 3.8 Hz, 2H), 7.27 – 7.21 (m, 2H), 6.39 (d, J = 14.1 Hz, 2H), 4.26 (t, J = 5.1 Hz, 4H), 3.95 (t, J = 5.1 Hz, 4H), 3.03 (t, J = 7.5 Hz, 2H), 2.66 (s, 4H), 2.46 (s, 2H),1.90 (d, J = 6.4 Hz, 2H), 1.76 (s, 12H). ^{13}C NMR (101 MHz, Methanol-d_4): δ174.90, 174.90, 158.23, 147.33, 144.27, 142.43, 134.86, 129.66, 126.14, 123.37, 112.29, 102.79, 60.05, 50.57, 47.95, 35.33, 39.03, 28.50, 27.26, 22.30. ESI-MS m/z: 613.2 $[M]^+$; HR-MS m/z: 613.3100 (Calc. 613.3095) $[M]^+$, $C_{37}H_{45}N_2O_4S^+$.

Lip-Cy7S. The intermediate Cy7S (61 mg, 0.1 mmol), N, N'-dicyclohexylcarbodiimide (DCC, 62 mg, 0.3 mmol), 4-dimethylaminopyridine (DMAP, 37 mg, 0.3 mmol) and lipoic acid (103 mg, 0.5 mmol) were dissolved in anhydrous DMF and stirred in dark at r.t. for 18 h. The solution was removed to obtain the crude product and then purified via silica gel chromatography with the gradient of CH_2Cl_2/CH_3OH (from 50: 1 to 5: 1) to give pure Lip-Cy7S as a dark green solid. ^1H NMR (400 MHz, DMSO-d_6) δ (ppm): 8.75 (d, J = 14.1 Hz, 2H), 7.59 (d, J = 7.4 Hz, 2H), 7.50

– 7.37 (m, 4H), 7.26 (t, *J* = 7.0 Hz, 2H), 6.43 (d, *J* = 14.2 Hz, 2H), 4.54 (t, *J* = 4.8 Hz, 4H), 4.46 (t, *J* = 4.8 Hz, 4H), 3.46 (dq, *J* = 8.9, 6.2 Hz, 2H), 3.16 – 3.00 (m, 4H), 2.97 (t, *J* = 7.1 Hz, 2H), 2.67 (s, 4H), 2.48 (s, 2H), 2.33 (dq, *J* = 12.5, 6.2 Hz, 2H), 2.10 (t, *J* = 7.5 Hz, 4H),1.84 (s, 2H), 1.77 (dt, *J* = 12.9, 6.7 Hz, 2H), 1.68 (s, 12H), 1.55 – 1.38 (m, 4H), 1.34 – 1.26 (m, 4H), 1.18 (q, *J* = 7.6 Hz, 4H). ^{13}C NMR (101 MHz, DMSO-d_6) δ (ppm): 172.72, 172.45, 172.45, 155.71, 145.20, 142.16, 140.73, 133.15, 128.35, 124.84, 122.36, 111.26, 101.81, 60.53, 55.87, 50.57, 48.82, 43.02, 38.06, 35.22, 33.92, 33.22, 33.00, 27.96, 27.33, 25.76, 23.79, 20.53. ESI-MS m/z: 990.2 [M+H]$^+$; HR-MS m/z: 989.3759 (Calc. 989.3754) [M]$^+$, $C_{53}H_{69}N_2O_6S_5^+$.

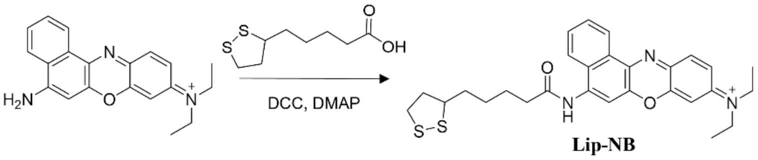

Supplementary Scheme 2 | Synthesis of Lip-NB.

Synthesis of *Lip-NB*. Nile blue (83 mg, 0.2 mmol), O-(7-azabenzotriazol-1-yl)-N,N,N′,N′-tetramethyluronium hexafluorophosphate (HATU, 91 mg, 0.24 mmol), N,N-Diisopropylethylamine (DIPEA, 39 mg, 0.3 mmol) and lipoic acid (103 mg, 0.5 mmol) were dissolved in anhydrous CH_2Cl_2 and vigorously stirred at r.t. for 24 h. The reaction solution was filtered to remove the undissolved solid, and the filtrate was evaporated and chromatographed on silica gel with gradient of CH_2Cl_2/CH_3OH (changed from 100: 1 to 10: 1) to afford Lip-NB as a blue powder. ^{1}H NMR (400 MHz, DMSO-d_6) δ 10.70 (s, 1H), 8.94 (d, J = 8.8 Hz, 1H), 8.66 (s, 1H), 8.29–7.70 (m, 4H), 7.43 (s, 1H), 3.94 (s, 4H), 3.67 (dq, J = 8.6, 6.1 Hz, 1H), 3.26–3.08 (m, 2H), 2.74 (t, J = 7.5 Hz, 2H), 2.44 (dt, J = 12.4, 6.2 Hz, 1H), 1.90 (dq, J = 13.4, 6.8 Hz, 1H), 1.82–1.63 (m, 4H), 1.50 (q, J = 7.6 Hz, 2H), 1.33 (t, J = 7.0 Hz, 6H). ESI-MS m/z: 506.2 [M]$^+$; HR-MS m/z: 506.1935 (Calc. 506.1930) [M]$^+$, $C_{28}H_{32}N_3O_2S_2^+$.

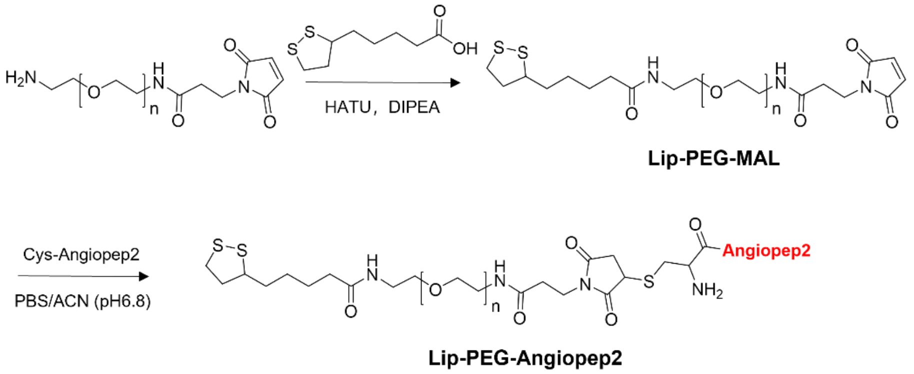

Supplementary Scheme 3 | Synthesis of Lip-PEG-Angiopep2.

Synthesis of *Lip-PEG-MAL*. A mixture of NH_2-PEG-Mal (500 mg, 0.1 mmol), HATU (190 mg, 0.5 mmol), DIPEA (65 mg, 0.5 mmol) and lipoic acid (103 mg, 0.5 mmol) in 10.0 mL anhydrous DMF was stirred thoroughly at r.t. for 24 h. Lip-PEG-MAL was purified by dialyzing against ultrapure water followed by lyophilization.

Synthesis of *Lip-PEG-Angiopep2*. Coupling of Lip-PEG-MAL (52 mg, 10 μmol) and cysteine-modified angiopep2 peptide (24 mg, 10 μmol) was carried out in a mixture solution of acetonitrile/PBS (0.01 M, pH 7.4) (15:85 V/V) at r.t. Lip-PEG-Angiopep2 was purified by dialyzing against ultrapure water followed by lyophilization.

Radio-synthesis of ^{99m}Tc-ultraHOCls. Thiol diethylenetriaminepentaacetic acid (DTPA) derivative was synthesized according to the previous work with minor modification[2]. Briefly, a mixture of mercaptoethylamine (3.8 mg, 50 μmol), and DTPA dianhydride (36 mg, 0.1 mmol) in 5.0 mL anhydrous DMF was stirred thoroughly with TEA (10 mg, 0.1 mmol) at r.t. for 12 h, and the reaction solution was used for subsequent reactions without any processing. DTPA-modified ultraHOCls was synthesized with a similar procedure as ultraHOCls but added an appropriate amount of reaction solution containing the above thiol-DTPA derivative. For the radiolabeling of ^{99m}Tc, DTPA-modified ultraHOCls and stannous chloride ($SnCl_2$, 100 μg, pH 2.0) were added to 2 mL PBS (pH 6.5) and vortexed. Then we added freshly eluted ^{99m}Technetium pertechnetate (0.2–0.5 mL, ~200 MBq) to the above mixture solution and incubated at 50 °C for at least 30 min. The mixed solution was purified by centrifugation (11000 rpm, 15 min) three times to remove unlabeled ^{99m}Tc. We determined the radiochemical purity of ^{99m}Tc-ultraHOCls by paper chromatography with Xinhua No.1 filter paper and utilized saline as the mobile phase. The sheets were analyzed with a gamma counter (SN-684, Shanghai Hesuo Rihuan Photoelectric Instrument, China) and high-performance storage phosphor screen (Cyclone; Canberra-Packard, Ontario, Canada).

Transmission electron microscopy (TEM). For the observation of morphology and size of ultraHOCls, TEM, high-resolution TEM (HRTEM) images and selected area electron diffraction (SAED) patterns were recorded on a JEOL 2100F (JEOL) field emission. We spotted sample aliquots on a copper grid coated with amorphous carbon and removed the excess liquid by wicking it with filter paper. The grids were then air-dried at r.t. Images of the ultraHOCls were captured using TEM operating at 300 kV and processed with the DigitalMicrograph software (Version 1.71.38). Freshly resected brain tissues were immersed into ice-cold glutaraldehyde fixing solution (special for the electron microscope, 2.5%, pH 7.2–7.4) at 4 °C. Samples were stored at 4 °C till analysis. The tissues were dehydrated, paraffin-embedded, sectioned (60–80 nm) and placed on 150 meshes cuprum grids with formvar film. TEM images were taken on a

Hitachi TEM (HT7800, Hitachi, Japan).

Dynamic light scattering (DLS). The size distributions and Zeta potential (ζ-potential) of nanoparticles were measured in disposable Zeta potential cells using Malvern Zetasizer (ZS90, Malvern Instruments Ltd., UK) at 25 °C. ζ-potential was calculated by the Zetasizer software (Version 7.11) using the Smoluchowski model.

Tissue penetration depth study. Fixed porcine muscles of 0–3.5 mm thickness were placed on the top of a solution containing ultraHOCls for the Raman penetration depth measurements. The Raman intensities of ultraHOCls were obtained by quantifying the peak 518 cm^{-1}.

Preparation of various radical species. The hypochlorite (OCl^{-}) solution was delivered from a commercial NaOCl solution (4–5%). The H_2O_2 solution was delivered from a commercial solution (30%). The superoxide radical anion (O_{2}-•) solution was prepared by dissolving commercially available KO_2 in DMSO. We prepared the •OH solution by the Fenton reaction from iron (II) chloride ($FeCl_2$) and H_2O_2. We obtained the peroxyl radicals (ROO•) solution by diluting commercially available tert-Butyl hydroperoxide (t-BuOOH) in water. Equal amounts of $NaMoO_4$ and H_2O_2 were mixed to yield $^1O_2$ of 10 mM. The NO solution was generated from sodium nitroferricyanide-(III) dehydrate in water.

Raman signal stability. We investigated the influence of storage time (0, 1, 2, 4, 8, 15, and 30 days) and the irradiation time (0, 1, 2, 5, 10, 30, 60, 120, 180, and 240 min) on the Raman signal stability of prepared ultraHOCls. The intensities of Raman bands at both 518 cm^{-1} and 586 cm^{-1} were measured at 4 random locations.

Radio-stability. We added 20 μL of ^{99m}Tc-ultraHOCls (~0.74 MBq) to 0.2 mL of PBS or mouse serum and incubated the mixed solution at 37 °C for 12 h. The radio-stability of ^{99m}Tc-ultraHOCls was determined at selected time points (0, 1, 4, 8, and 12 h) by paper chromatography.

Cytotoxicity. For *in vitro* toxicity evaluation, mouse primary microglial cells were cultured in 96-well plates at 37 °C for 12–24 h for adherence to the plates. The cells were refreshed with a culture medium containing gradient concentrations of ultraHOCls (from 0 to 4 nM) and incubated for 24 h. Subsequently, 10 μL CCK-8 reagent was added and co-cultured for another 4 h. We measured the optical density with a Synergy HTX Multi-Mode Reader (HTX, BioTek Gen5, Vermont) at 450 nm. For *in vivo* toxicity evaluation, we intravenously injected ultraHOCls into four healthy mice at a dosage of 800 nmol/kg, while another group of four mice injected with an equal volume of PBS was used as control. The mice were observed and weighed every few days for 28 d. The blood was collected at 28 d post-injection, and centrifugated to obtain the supernatant for biochemical analysis. The mice were euthanized and major viscera were harvested and stained with haematoxylin and eosin (H&E).

***In vitro* cellular uptake studies.** Primary microglial cells were seeded into 6-well-plates and incubated for 12–24 h for adherence to the plates. Then the media were supplemented with IFNγ (100 ng/mL) plus LPS (600 ng/mL) or isometric PBS. The media were refreshed with a culture medium containing ultraHOCls (0.4 nM) and incubated for 0.5, 2, 4 and 8 h. After washing with PBS three times, we collected the cells for Raman spectra acquisition.

Neuronal survival evaluation. Fluoro Jade B (FJB) staining studies were performed to identify degenerated neurons[3]. Briefly, the dewaxed paraffin sections (5 μm thickness) were rehydrated with an ethanol solution and potassium permanganate, followed by rinsing with ultrapure water. The sections were then stained with a solution containing 0.001% FJB. Images were captured using a META confocal laser scanning microscope (LSM 710, Carl Zeiss, Germany). We calculated the number of FJB-positive neuronal cells in the hippocampus. Nissl staining studies were performed to evaluate survived neurons. The 5-μm paraffin-embedded slices were de-waxed, hydrated, and then stained with 1% cresyl violet solution. After dehydrating with ethanol, washing with ultrapure water, and clearing with xylene, slices were sealed with neutral gum. We acquired the images with an optical microscope (Olympus BX51, Olympus, Japan) and counted the number of surviving intact hippocampal pyramidal cells.

***In vivo* SPECT/CT studies.** KA models (n = 4 for acute phase, n = 4 for chronic phase) and sham models (n = 4) were used for SPECT/CT imaging after injecting intravenously ^{99m}Tc-ultraHOCls (5.6−7.4 MBq) at 0.5, 2, and 12 h, respectively. Mice were anesthetized with 1−2% isoflurane during the scanning period. Small animal SPECT/CT scans were performed on a nanoScan@SC SPECT/CT system (Mediso Medical Imaging System, Hungary) equipped with four high-resolution conical collimators with multi-pinhole plates. Acquisition parameters of CT image: x-ray tube, 0.98 mA 50 kVp; exposure time, 300 ms; 720 projections in all. SPECT was acquired under the standard mode using the following parameters: energy peak, 140 keV; full width, 20%; resolution, 1 mm/pixel; matrix, 256 × 256; scan time, 30 s/projection; 128 projections in all. All acquired data were reconstructed and analyzed using dedicated fusion software (Version 3.00.021.000).

Bio-distribution studies. KA models (n = 12 for acute phase, n = 12 for chronic phase) and sham models (n = 12) were intravenously injected with ^{99m}Tc-ultraHOCls (1.85−5.55 MBq). The mice were sacrificed at 0.5, 2 and 12 h post-administration and tissues of interest were excised and weighed. We measured the radioactivity with a gamma counter (SN-684, Shanghai Hesuo

Rihuan Photoelectric Instrument Co., Ltd., Shanghai, China). The decay-corrected radioactivity was calculated and radioactivity uptake of ^{99m}Tc-ultraHOCls was expressed as the percentage of the injected dose per gram of tissue (% ID/g).

***In vivo* MRI studies.** The MRI studies were performed on a 7.0 T small animal MR scanner (PharmaScan; Bruker Biospin, Billerica, MA) with a 38-mm-internal-diameter transmit/receive quadrature volume radiofrequency coil. T2W images were acquired using a turbo-rapid acquisition with relaxation enhancement (RARE) sequences with the following parameters: time of repetition/time of echo = 2500/33 ms, acquisition matrix = 256 × 256; number of excitation = 4, field of view = 20 × 20 mm; number of slices = 9; slice thickness = 0.8 mm, rare factor = 8.

***In vivo* PET/CT studies.** For the ^{18}F-FDG experiment, mice were fasted for more than 6−12 h before image acquisition. PET/CT images were acquired with an Inveon micro-PET/CT (Preclinical Solutions; Siemens Healthcare Molecular Imaging, Knoxville, TN). Each mouse received 7.4 ± 0.3 MBq ^{18}F-FDG via the tail vein injection. Isoflurane (1−2%) in oxygen was used to anesthetize the mouse for the duration of imaging. The CT images were firstly acquired under the following parameters: 120 projections per bed position, 360° of rotation, 500 μA anode source transmitting 80 keV X-ray with an exposure time of 300 ms, X-ray detector of 3072 transaxial pixels × 2048 axial pixels. 15-min static PET scans were then acquired in list mode. The PET images were reconstructed using a Fourier rebinning and ordered subsets expectation maximization 3D algorithm. Reconstructed computed tomography and PET images were fused and analysed using Inveon Research Workplace software.

Accelerating rotarod test. The accelerating rotarod behavioral test was used for testing motor function (Yiyan Technology, China). The parameters used in the tests include start speed (1 rpm), acceleration (accelerate 0.5 rpm/s), and highest speed (40 rpm). Each mouse underwent four consecutive trials with a rest period of 30 min between each trial. The mean latency time to fall off the rotating rod for the last two trials was used for analysis.

Open field test. Anxiety-like behavior and locomotor activity were measured using an open field test. Mice were initially placed in one corner of the open field apparatus (40 cm length × 40 cm width × 35 cm height) (Noldus Information Technology, Netherlands) and recorded for 10 min. Total distance traveled, total velocity, velocity in the edge were used as measures of locomotor behavior. The entrance frequency, duration, and distance traveled in the center area (20 × 20 cm) were used as measures of anxiety-like behavior.

EPM test. The EPM test was performed to measure spontaneous locomotor and anxiety-related behavior in yet a second way. Mice have a natural tendency to actively explore a new environment, but fear open areas. The apparatus used for the EPM test consisted of two closed arms and two open arms (35 cm length × 5 cm width × 30 cm height) (Noldus Information Technology, Netherlands) joined perpendicularly and raised 1 m from the ground. Mice were individually placed in the center of the apparatus and were allowed to freely explore the EPM for 5 min. Quantification of total distance, total velocity, and the number of total entries were used for locomotor evaluation. The percentage of open arm entries, the number of entries in open arms, and the average duration in the open arms were analyzed for evaluating anxiety-related behavior.

Tail suspension test. The depression-like behavior was evaluated by a tail suspension test. Briefly, mice were suspended by fixing their tail with medical tape from a hook connected with the horizontal steel wire. The mice were hung upside down approximately 15 cm above the ground covered with a soft sponge panel. The activity of the tested mice was recorded for 6 min using a video camera and the immobility time was scored for the last 4 min of the session.

Y-Maze test. The spatial-dependent working memory was evaluated by the Y-Maze test. The theoretical basis of test is the innate tendency of rodents to alternate between exploring different arms of a Y-maze. The apparatus used for the test consisted of three closed arms [(35 cm (length) x 5 cm (width) x 25 cm (wall height)]. Mice were initially placed into the center of Y-maze and were allowed to freely explore the three arms of the maze for 5 min. Prefrontal cortex-dependent cognitive impairment was evaluated by quantification of the percentage of spontaneous alternation, spontaneous alternation, the number of incorrect alternations, the number of perseverations, the total number of arm entries, and total distance.

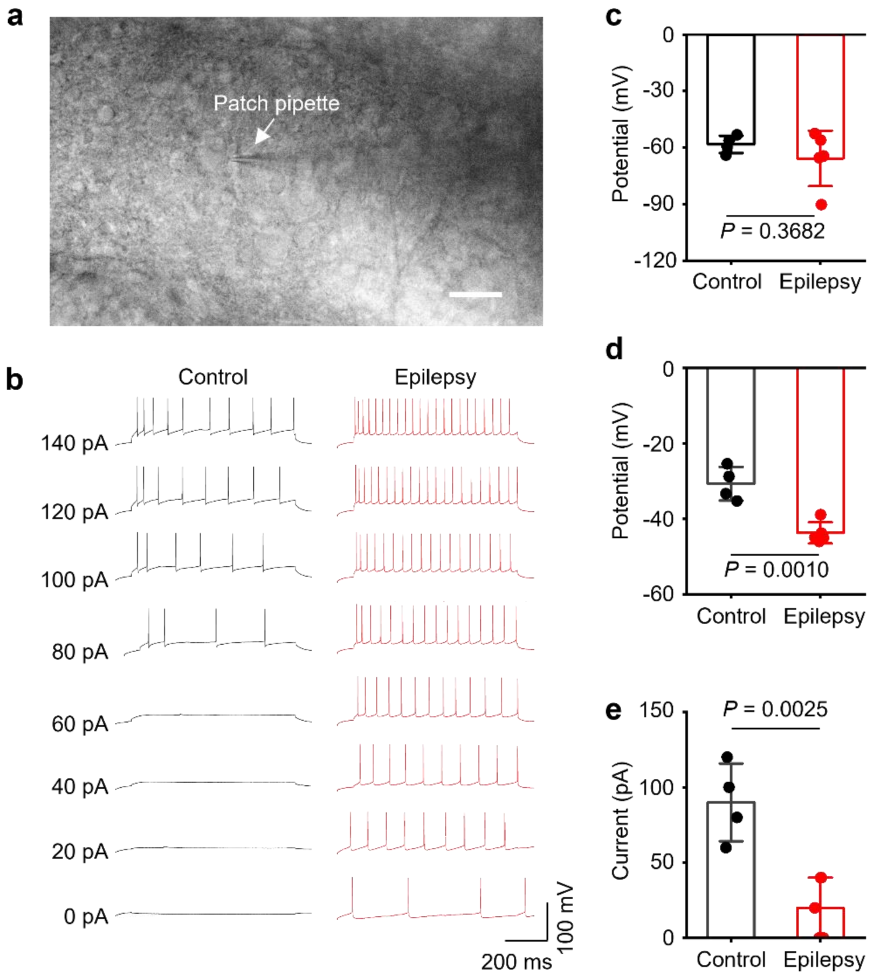

Supplementary figure 1 | Neuron hyperexcitability is recorded from the resected brain tissues from DRE patients. a, A bright-field image of a patch pipette attached to the membrane of the neuron in neocortical slices derived from a 22-year-old DRE patient with complex partial seizure. Scale bar, 50 μm. **b,** Representative action potential (AP) trains induced by injecting increased currents (from 0-pA to 140-pA with an increment of 20 pA). **c–e**, Statistical analysis of resting membrane potential (**c**), AP threshold (**d**) and rheobase (**e**) recorded in resected brain tissues derived from patients with DRE and patients without a history of seizures. Data are presented as the mean ± s.d. (n = 4 for control patients, n = 5 for epileptic patients). *P* values were analysed by two-tailed unpaired Student's *t*-tests.

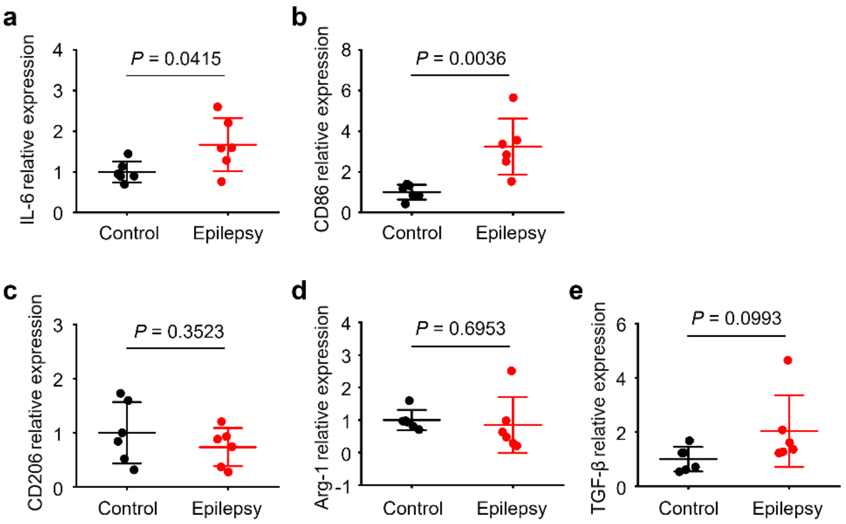

Supplementary figure 2 | mRNA expression of phenotypic markers in epileptic and control brain tissues. a–e, Relative mRNA expression of proinflammatory cytokines IL-6 (**a**) and biomarker CD86 (**b**), anti-inflammatory biomarker CD206 (**c**), anti-inflammatory cytokines Arg-1(**d**) and TGF-β (**e**) in resected brain tissues from DRE patients and patients without a history of seizures (n = 6 biologically independent experiments). Data are presented as the mean ± s.d. *P* values were analysed by two-tailed unpaired Student’s *t*-tests.

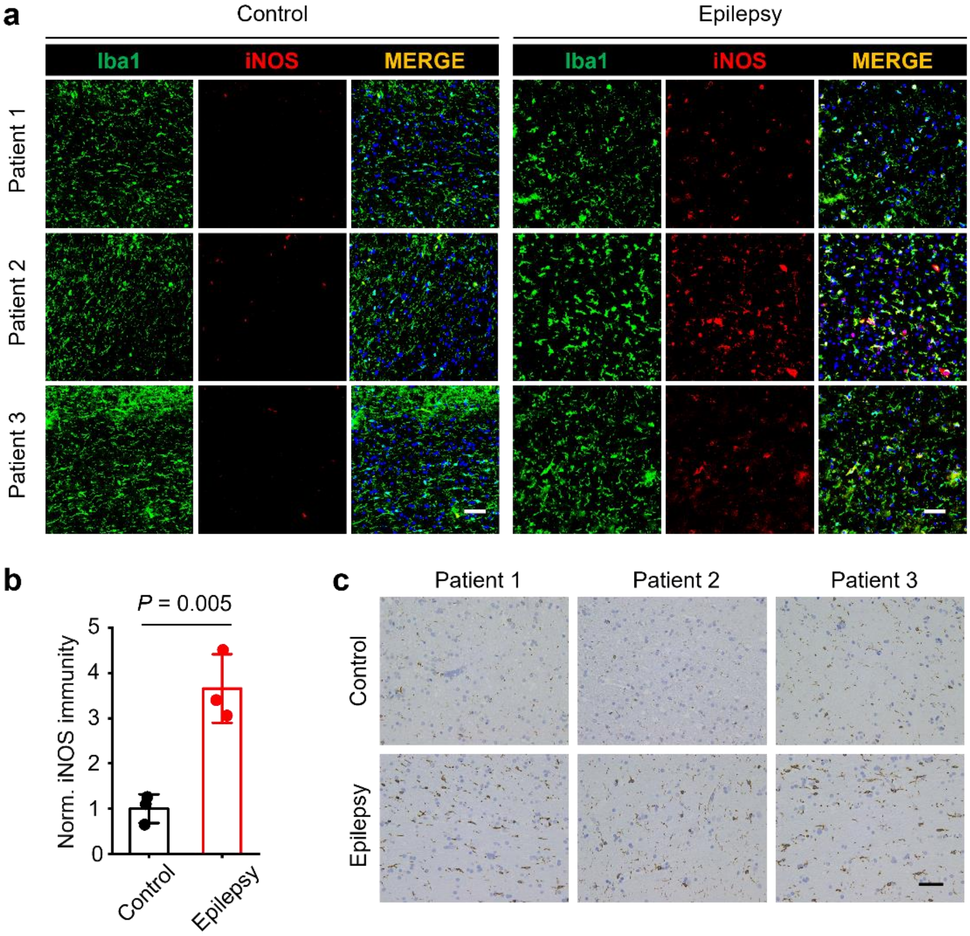

Supplementary figure 3 | Proinflammatory microglia are found in the lesions of DRE patients. a, Coimmunostaining for Iba1 and iNOS in human surgically resected tissues. Scale bar, 50 μm. **b,** Quantification of iNOS staining in Iba1-positive microglia by ImageJ (n = 3 biologically independent experiments). **c,** Immunohistochemistry of Iba1 in excised tissues from patients with DRE and patients without a history of seizures. Scale bar, 50 μm. Data are presented as the mean ± s.d. *P* values were analysed by two-tailed unpaired Student's *t*-test.

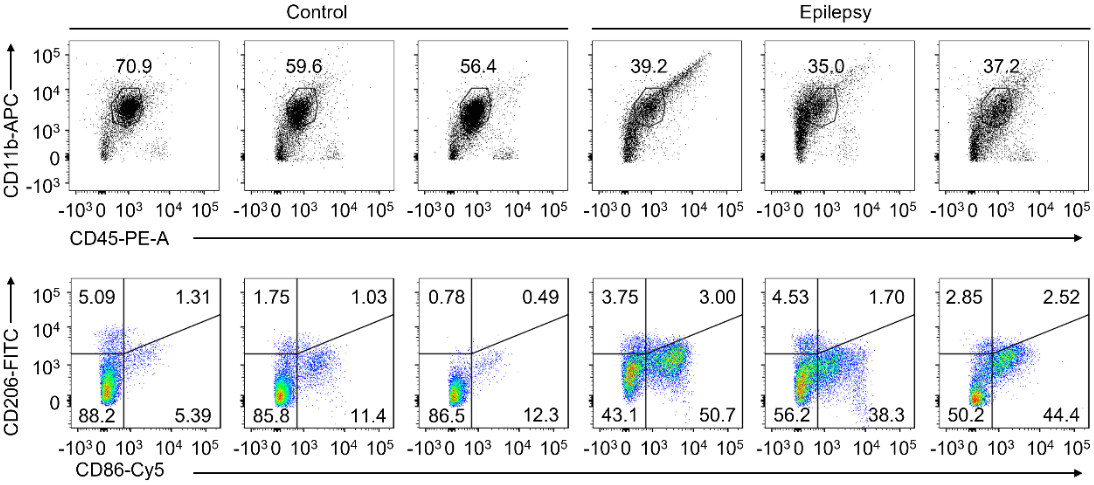

Supplementary figure 4 | Proinflammatory microglia activation is found in the lesions of DRE patients. Flow cytometry images of microglia ($CD11b^{+}CD45^{mid+}$) and pro-inflammatory microglia ($CD86^{+}CD11b^{+}CD45^{mid+}$) in resected brain tissues from DRE patients and patients without a history of seizures (n = 3 biologically independent samples).

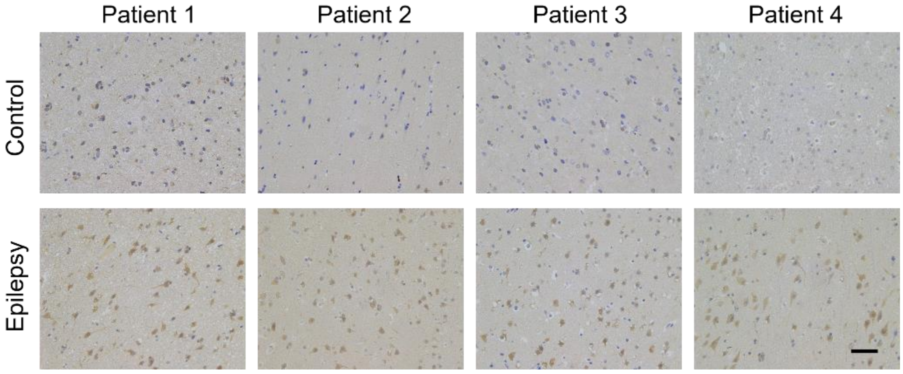

Supplementary figure 5 | Upregulated MPO expression is found in the lesions of DRE patients. Immunohistochemistry images of MPO in excised tissues from patients with DRE and patients without a history of seizures. Scale bar, 50 μm.

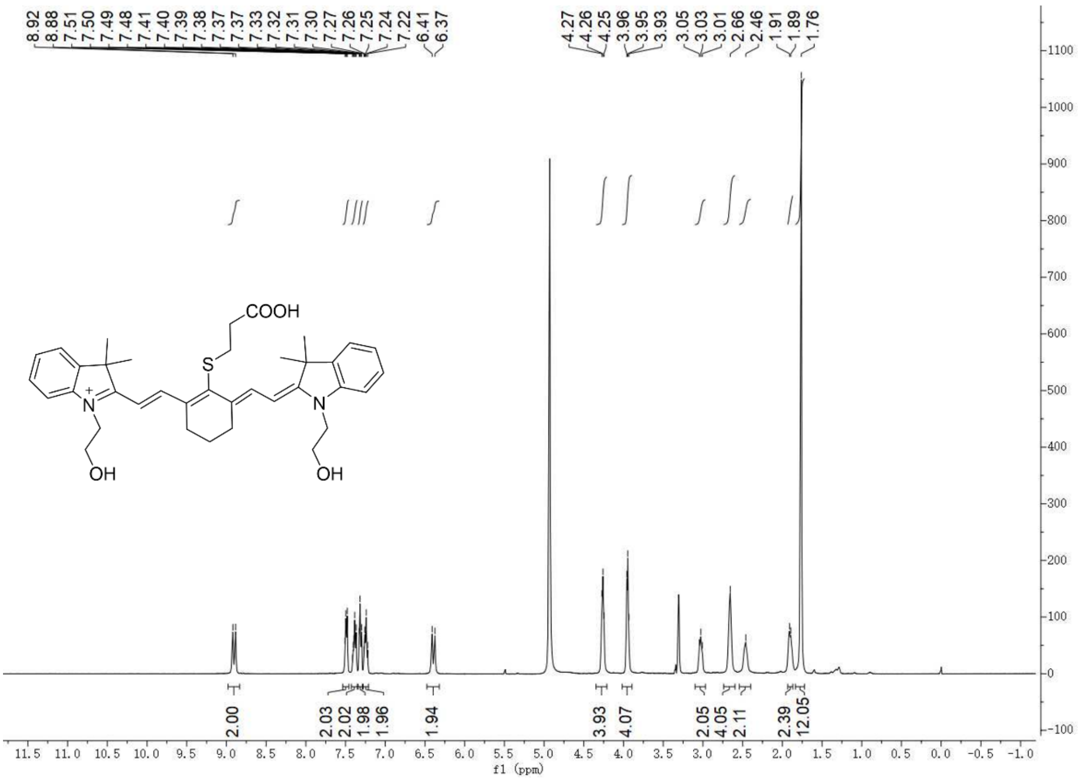

Supplementary figure 6 | ^{1}H NMR spectrum of Cy7S in CD_3OD.

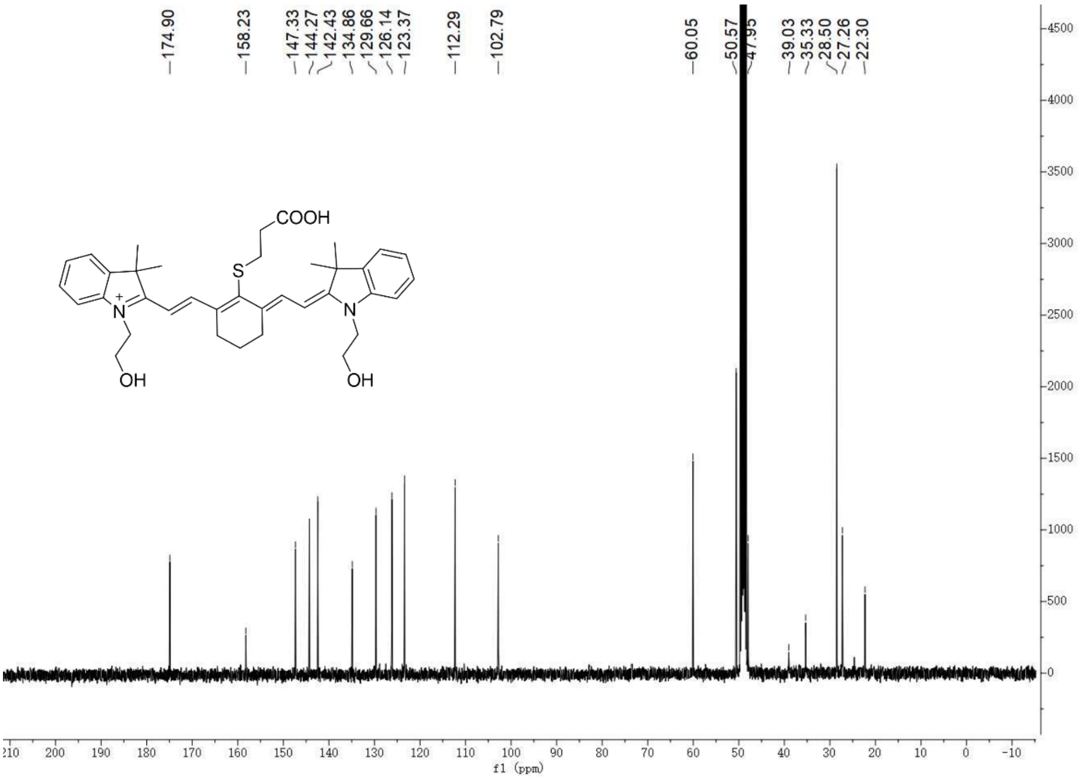

Supplementary figure 7 | ^{13}C NMR spectrum of Cy7S in CD_3OD.

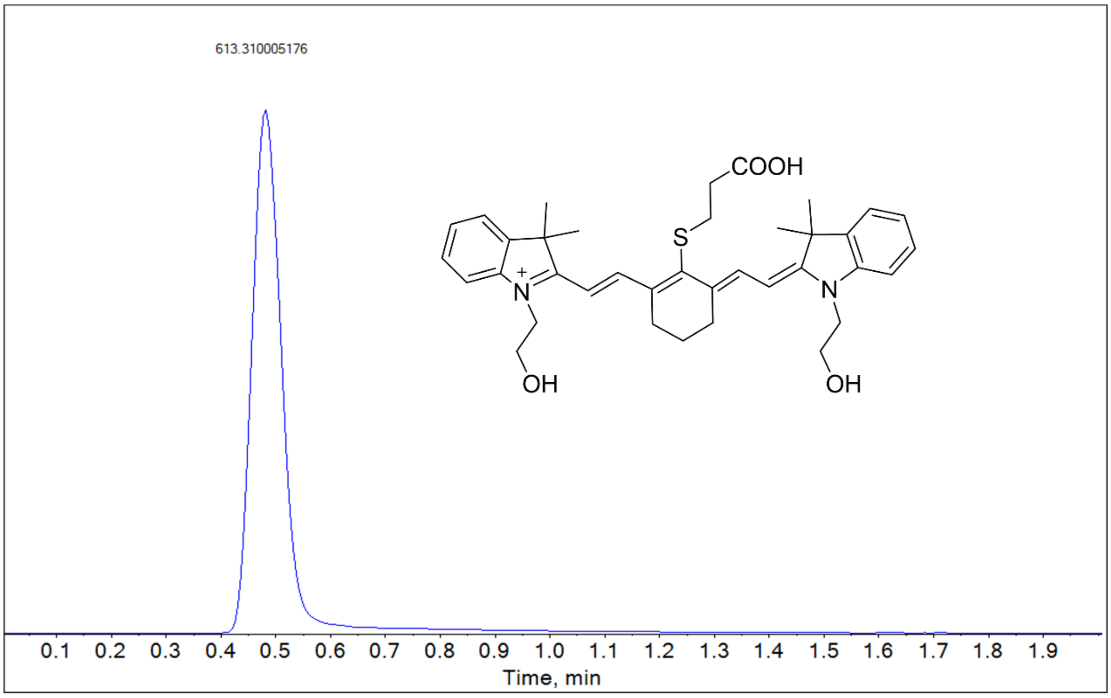

✓✓✓✓✓	Compound Name (Library Hit)	Score	Formula	Intensity	Threshold	Expected m/z	Found at m/z	Error (ppm)	Expected RT (min)	Found RT (min)	RT Delta (min)	Isotope Diff (%)	Library Score (%)
	613.310005176	98%	C37H45 N2O4S	588373	5	613.3095	613.3094	-0.2	0.00	0.48	0.48	2.8%	N/A

Supplementary figure 8 | High-resolution mass spectrum of Cy7S.

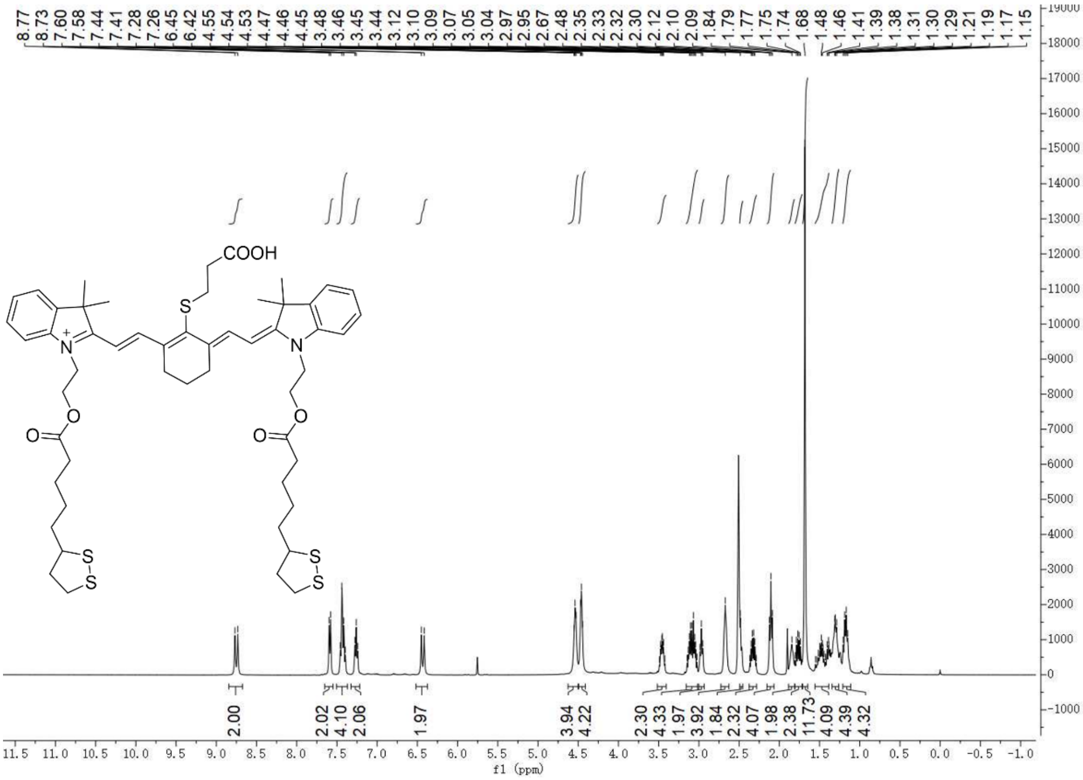

Supplementary figure 9 | ^{1}H NMR spectrum of Lip-Cy7S in DMSO-*d*$_6$.

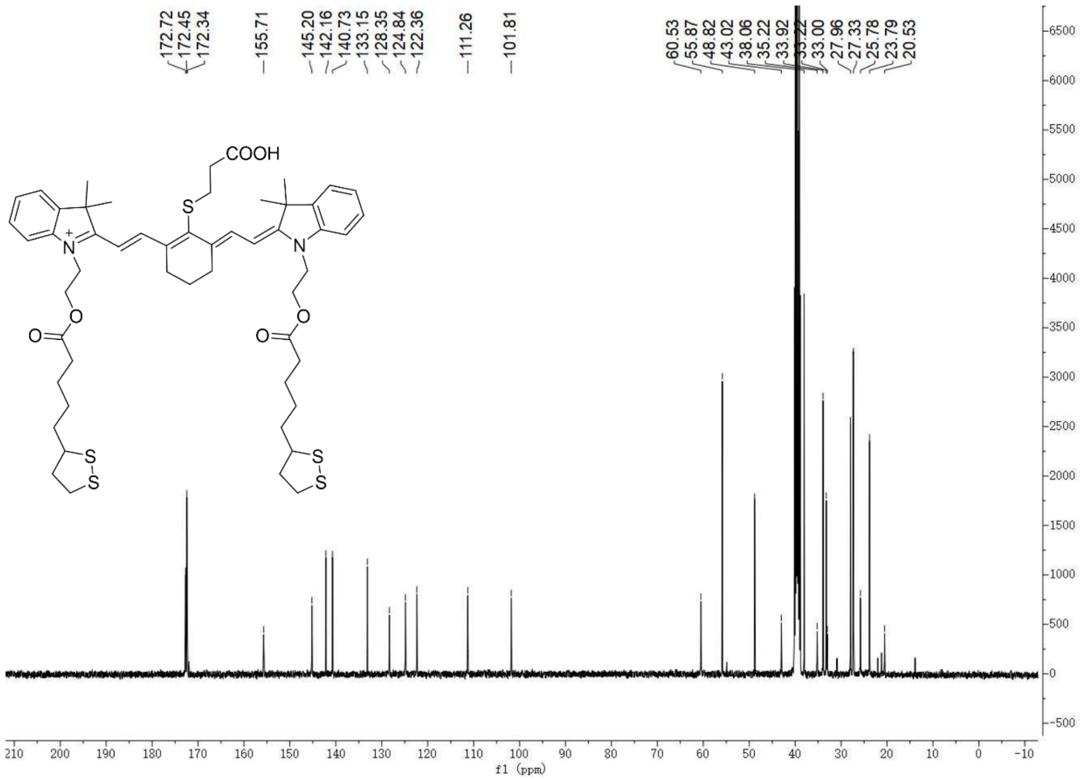

Supplementary figure 10 | ^{13}C NMR spectrum of Lip-Cy7S in DMSO-*d_6*.

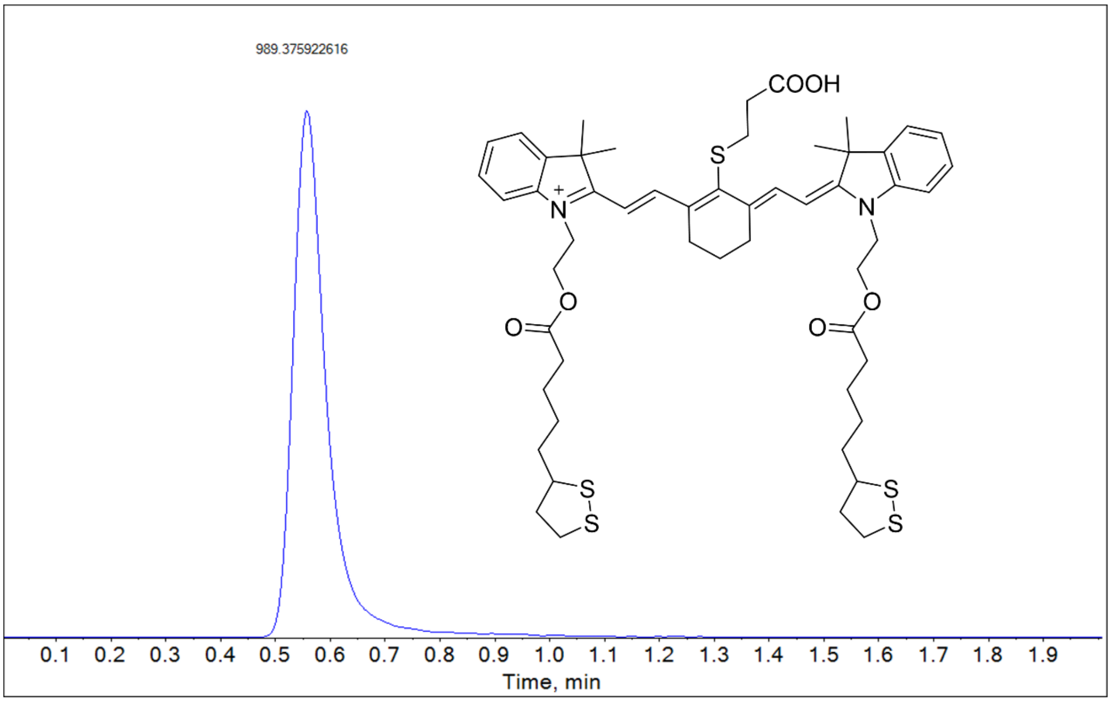

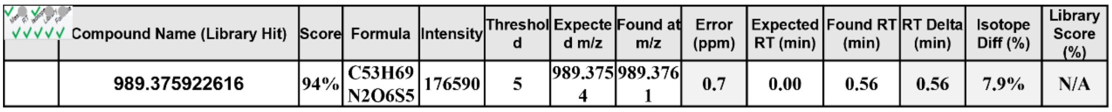

✓✓✓✓✓	Compound Name (Library Hit)	Score	Formula	Intensity	Threshold	Expected m/z	Found at m/z	Error (ppm)	Expected RT (min)	Found RT (min)	RT Delta (min)	Isotope Diff (%)	Library Score (%)
	989.375922616	94%	C53H69N2O6S5	176590	5	989.3754	989.3761	0.7	0.00	0.56	0.56	7.9%	N/A

Supplementary figure 11 | High-resolution mass spectrum of Lip-Cy7S.

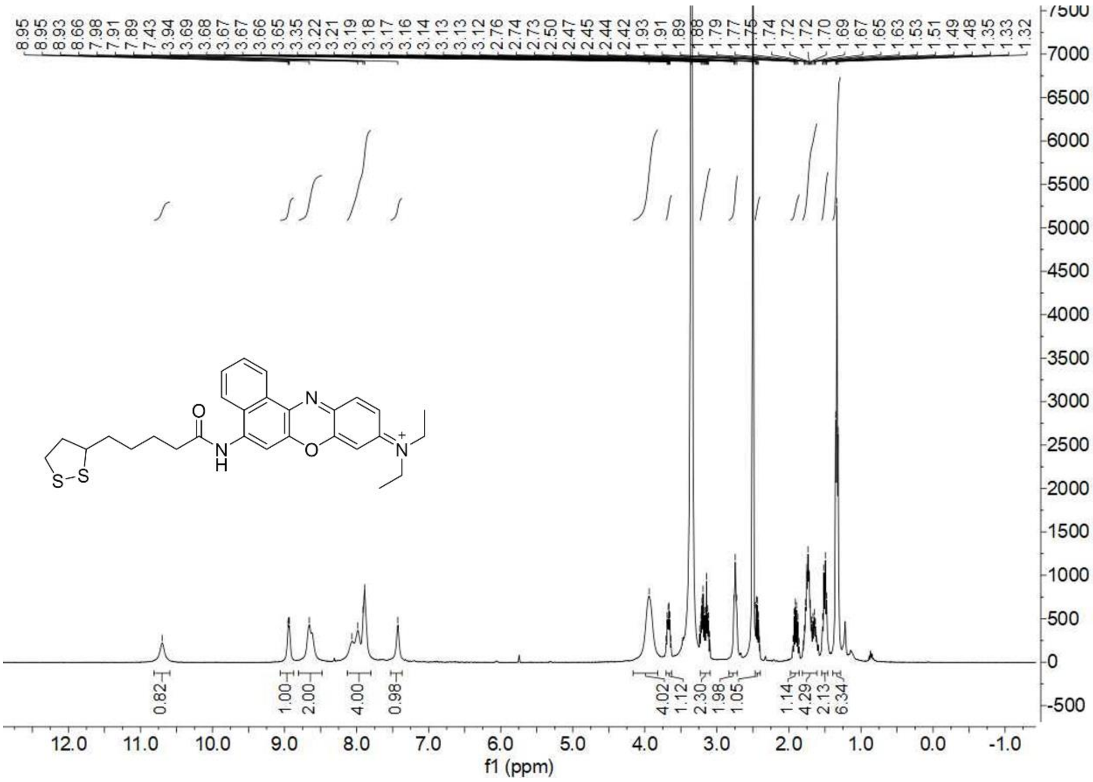

Supplementary figure 12 | ^{1}H NMR spectrum of Lip-NB in DMSO-d_6.

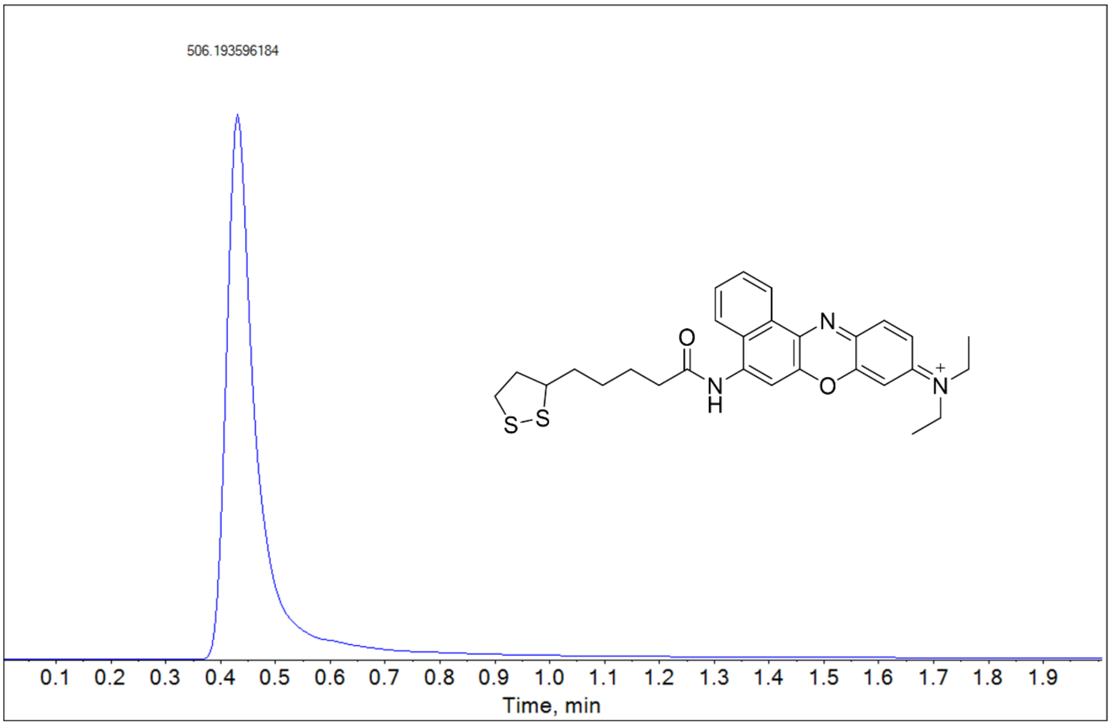

✓✓✓✓✓	Compound Name (Library Hit)	Score	Formula	Intensity	Threshold	Expected m/z	Found at m/z	Error (ppm)	Expected RT (min)	Found RT (min)	RT Delta (min)	Isotope Diff (%)	Library Score (%)
	506.193596184	95%	C28H32N3O2S2	2970718	5	506.1930	506.1934	0.6	0.00	0.43	0.43	3.4%	N/A

Supplementary figure 13 | High-resolution mass spectrum of Lip-NB.

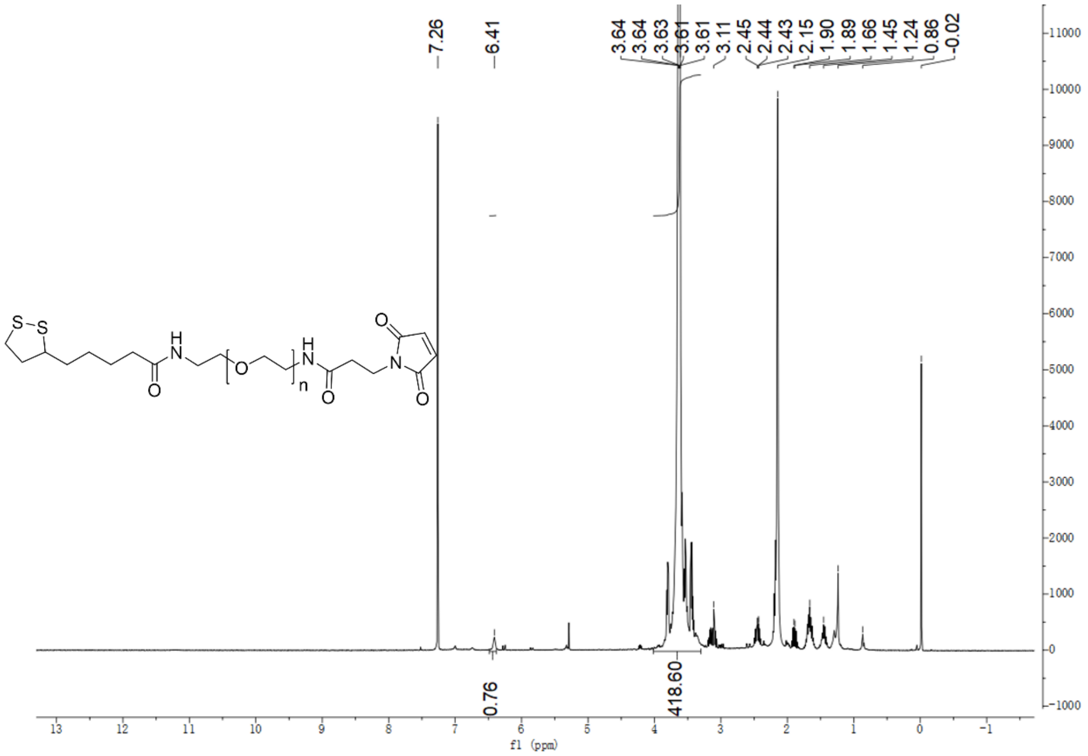

Supplementary figure 14 | ^{1}H NMR spectrum of Lip-PEG-MAL in $CDCl_3$.

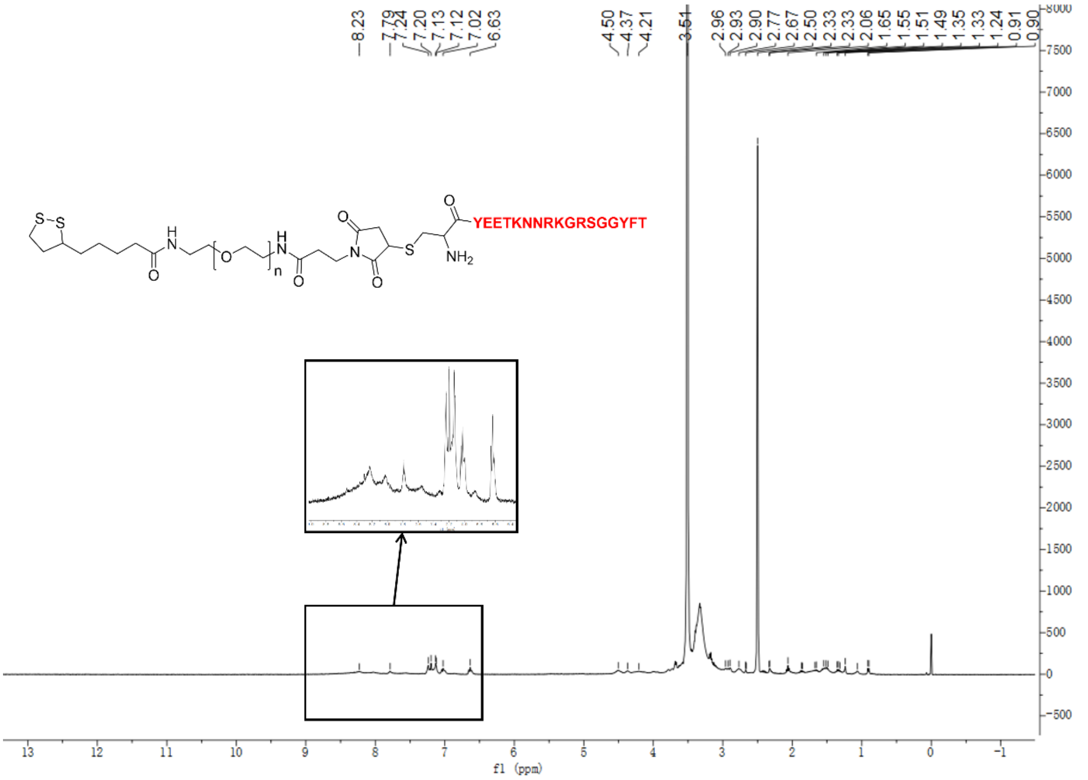

Supplementary figure 15 | ^{1}H NMR spectrum of Lip-PEG-Angiopep2 in DMSO-*d*$_6$. Insert highlights the characteristic peaks of angiopep2.

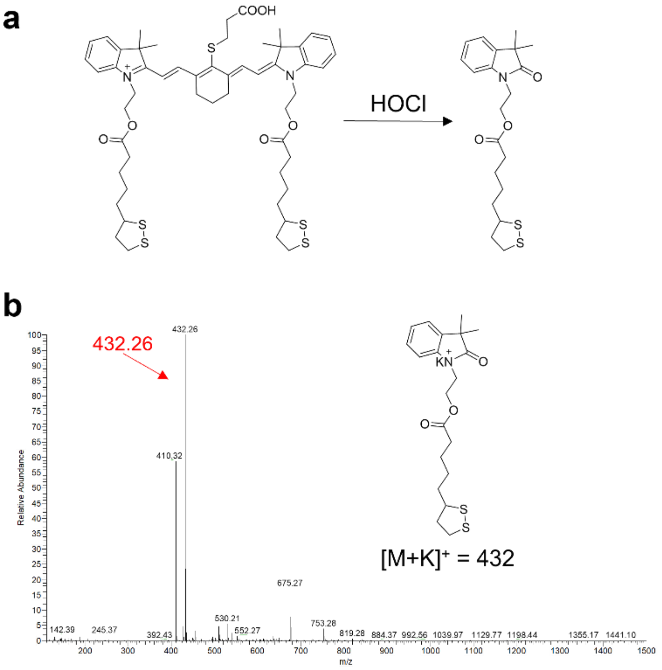

Supplementary figure 16 | HOCl triggered cleavage of Raman reporter molecule Lip-Cy7S. **a,** The proposed response mechanism of Lip-Cy7S inferred from the structural degradation. **b,** HPLC-MS spectrum of the reaction mixture. Upon treatment with HOCl, a new mass peak appeared at m/z 432.26 $[M+K]^+$, indicating the cleavage of the polymethine chain of Lip-Cy7S.

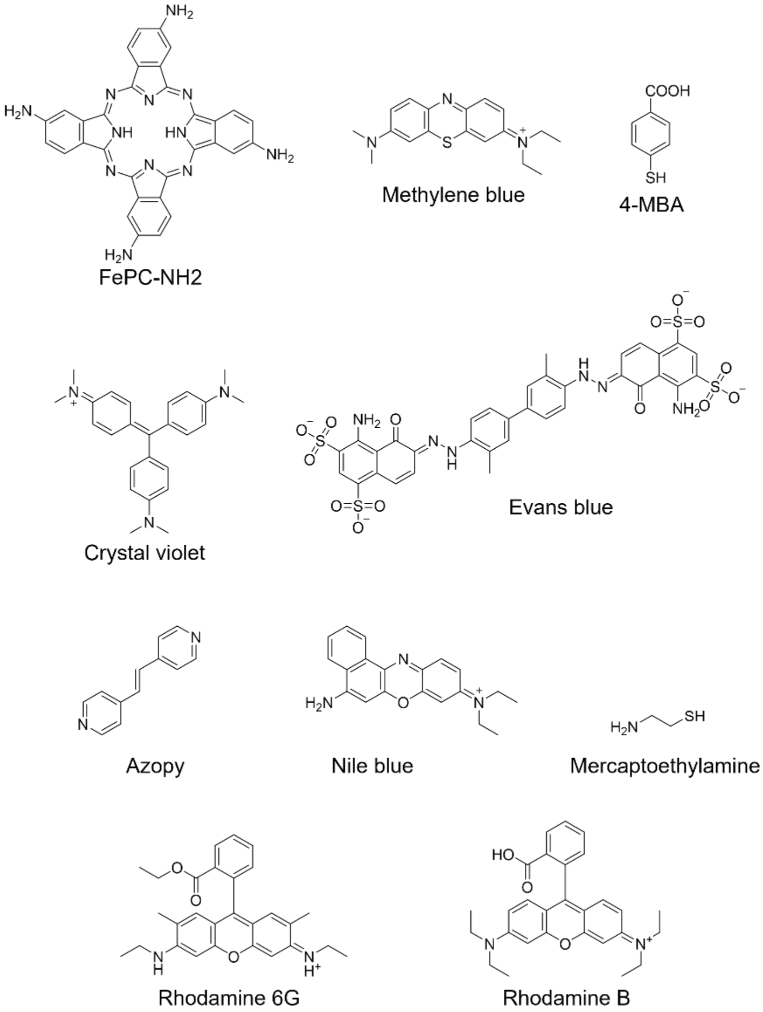

Supplementary figure 17 | Chemical structures of the molecules screened as a reference Raman reporter in this study.

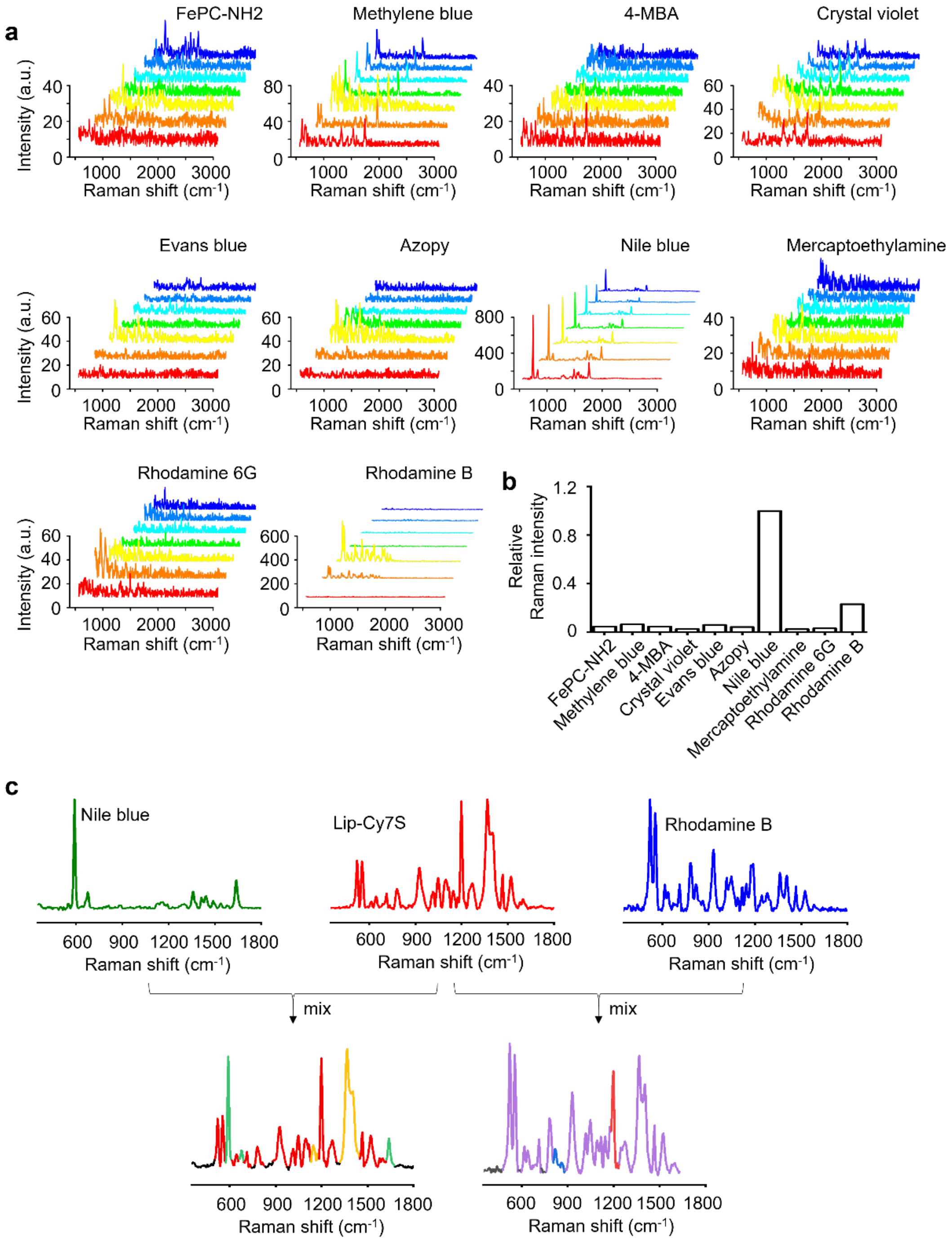

Supplementary figure 18 | Screening Raman reporter molecules as a built-in inner reference. a, Raman spectra of the screened molecules with various concentrations. **b,** Statistical analysis of SERS intensity shows the Au star with Nile blue and Rhodamine B generated higher Raman signals than other Reporters. **c,** Screening of Raman reporter molecules with non-overlapping peaks with Lip-Cy7S. The Raman spectrum of Lip-Cy7S, Nile blue and Rhodamine B were shown in red, green and blue, respectively (Upper). Mixed Raman spectrum of reporter Nile blue and reporter Rhodamine B with Lip-Cy7S, respectively (Bottom). The overlapping Raman peaks of Lip-Cy7S with reporter Nile blue were shown in yellow. The overlapping Raman peaks of Lip-Cy7S with Reporter Rhodamine B were shown in purple. Reporter Nile blue exhibits a non-overlapping Raman spectrum with Lip-Cy7S.

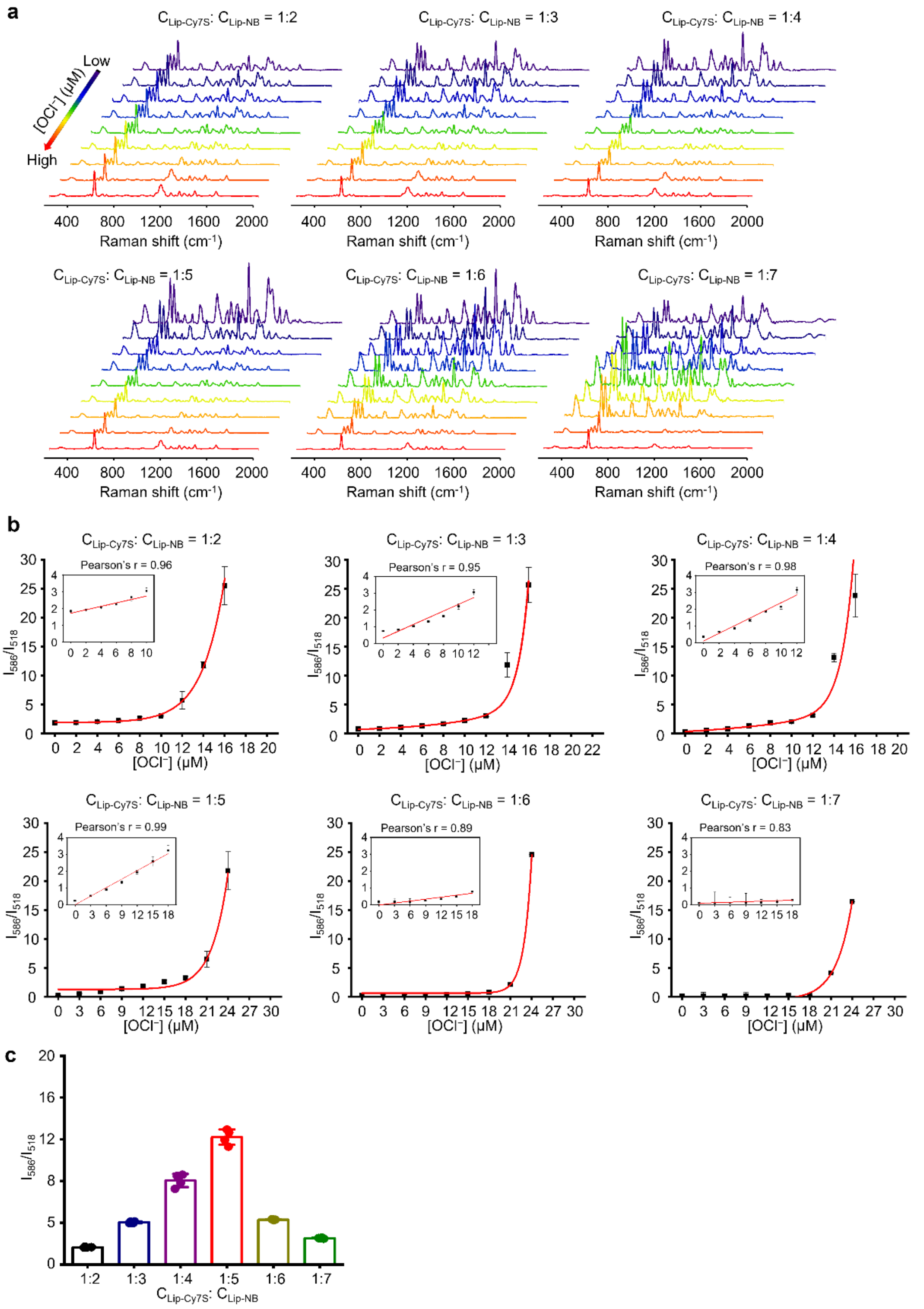

Supplementary figure 19 | The ratio between Lip-Cy7S and Lip-NB plays an important role in the performance for sensing HOCl. a, Raman spectrum of various Raman reporter ratios (Lip-Cy7S/Lip-NB = 2, 3, 4, 5, 6, 7) after the addition of OCl^- at various concentrations. **b,** Plots of Raman intensity ratios (I_{586}/I_{518}) versus concentrations of OCl^- with various Raman reporter ratios. Inset shows the linear response to lower OCl^- concentrations. **c,** Quantification of linear range for sensing OCl^- with various Raman reporter ratios. Data are presented as the mean ± s.d. (n = 3).

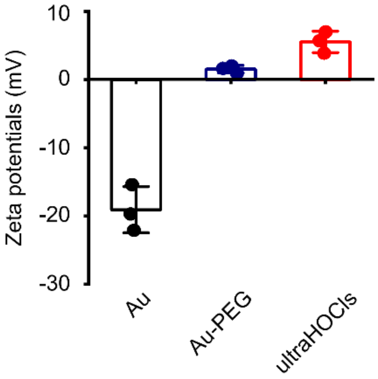

Supplementary figure 20 | The surface charges of each nanoformulation. The zeta potential of naked gold nanostar, gold nanostar modified with PEG and the HOCl ratiometric SERS nanosensor ultraHOCls. Au, gold nanostar.

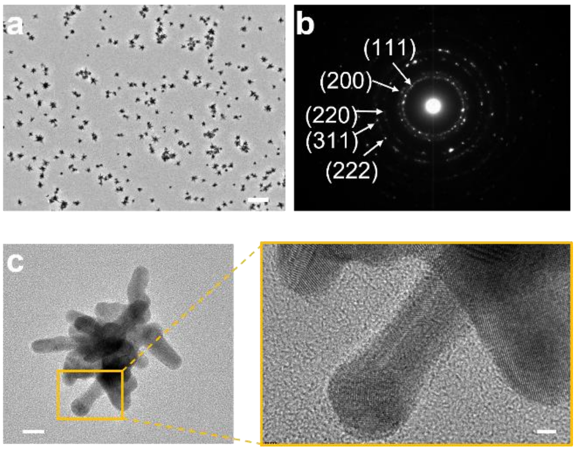

Supplementary figure 21 | Characterization of ultraHOCls. a, TEM images of the as-prepared ultraHOCls. Scale bar, 200 nm. **b,** SAED patterns of the ultraHOCls show the (111), (200), (220), (311), and (222) reflections of gold. **c,** High-resolution TEM images of ultraHOCls. Scale bar for left, 10 nm; Scale bar for right, 2 nm.

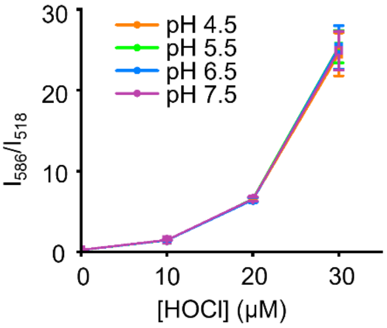

Supplementary figure 22 | Sensitivity of ultraHOCls to HOCl is pH-independent. Normalized I_{586}/I_{518} values of ultraHOCls at pH 4.5, 5.5, 6.5 and 7.5 against different concentrations of HOCl (from 0 to 30 μM). Data are presented as the mean ± s.d. (n = 4).

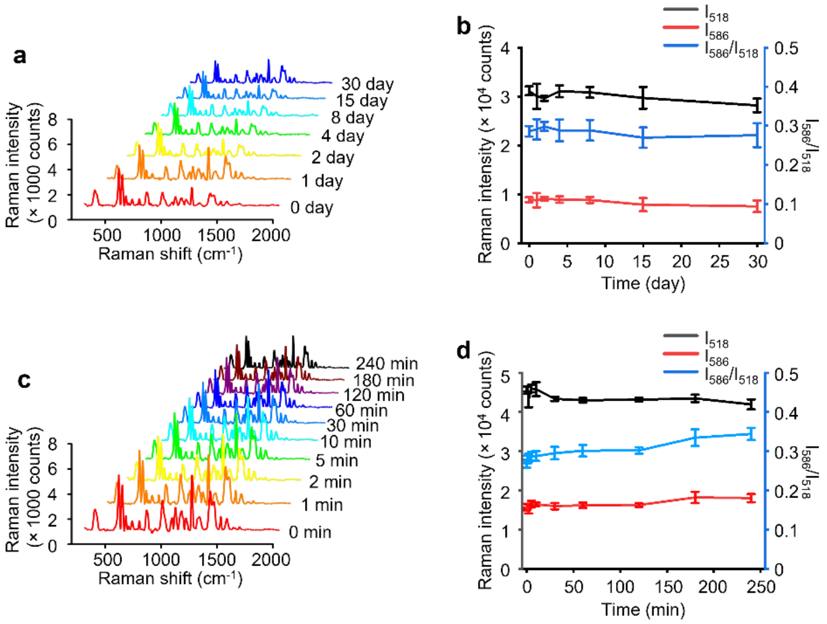

Supplementary figure 23 | UltraHOCls shows long shelf life and high photostability. a, Raman spectra showing uncompromised storage stability of 1 nM ultraHOCls at 4 °C in one month. Spectra were acquired at selected time points. **b,** The intensity of 518 cm^{-1} peak, 586 cm^{-1} peak and the SERS intensity ratio (I_{586}/I_{518}) were plotted against incubation time showing excellent storage stability of ultraHOCls. **c,** Raman spectra showing photostability of 1 nM ultraHOCls during continuous irradiation (80 mW laser power) for 240 min. Spectra were acquired at selected time points. **d,** The intensity of 518 cm^{-1} peak, 586 cm^{-1} peak and the SERS intensity ratio (I_{586}/I_{518}) were plotted against irradiation time showing a high photostability of the ultraHOCls. Data are presented as the mean ± s.d. (n = 4).

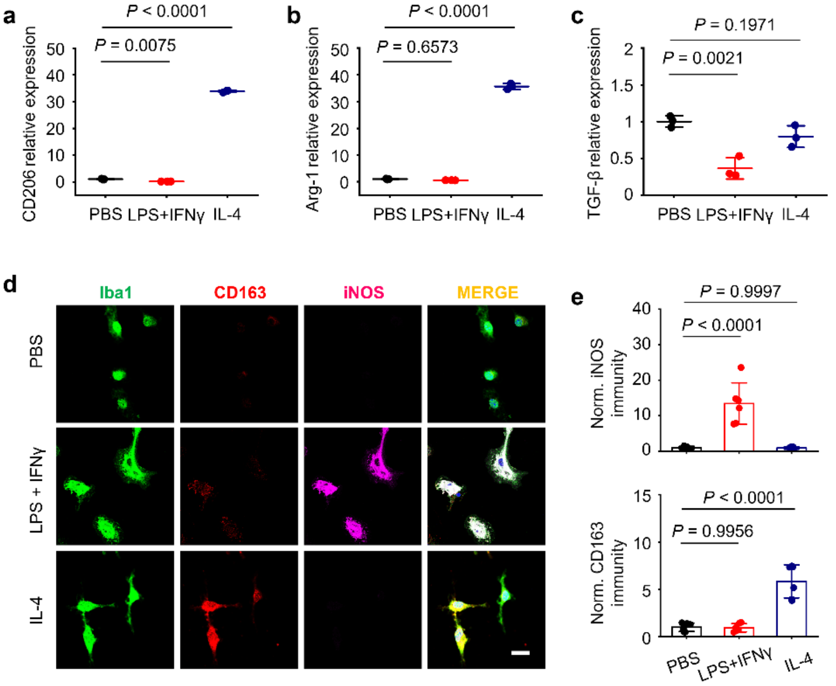

Supplementary figure 24 | Establishment of mouse primary microglia with different phenotypes. a–c, Relative mRNA expression of CD206 (**a**), Arg-1 (**b**) and TGF-β (**c**) in primary mouse microglia after treatment with LPS+IFNγ, IL-4 or isovolumetric PBS. **d,** Co-immunostaining for Iba1, iNOS, CD163, and DAPI counterstain in the primary cultures of mouse microglia after various treatments. Scale bar, 20 µm. **e,** Quantification of iNOS and CD163 staining in Iba1-positive microglia by ImageJ. All values are presented as the mean ± s.d of biologically independent samples with n = 3 (**a–c**) and n = 6 (**d,e**). *P* values were analysed by one-way ANOVA with Tukey's post-hoc test.

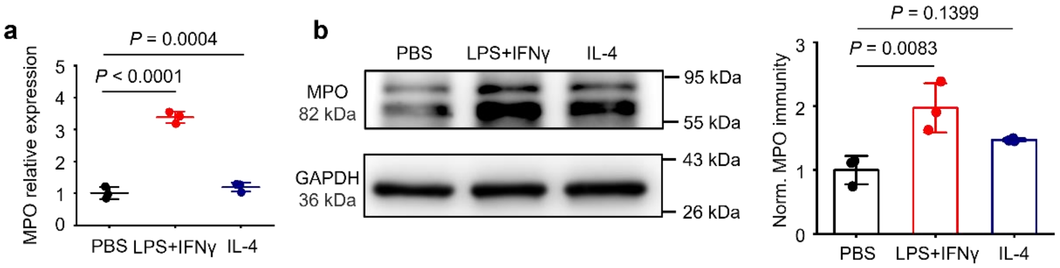

Supplementary figure 25 | Upregulation of MPO is found in proinflammatory microglia. a, Relative mRNA expression of MPO in primary mouse microglia after treatment with LPS+IFNγ, IL-4 or isovolumetric PBS. **b,** Immunoblots and quantification of the MPO in primary mouse microglia after treatment with LPS+IFNγ, IL-4 or isovolumetric PBS. Data are presented as the mean ± s.d. (n = 3 biologically independent experiments). *P* values were analysed by one-way ANOVA with Tukey's post-hoc test.

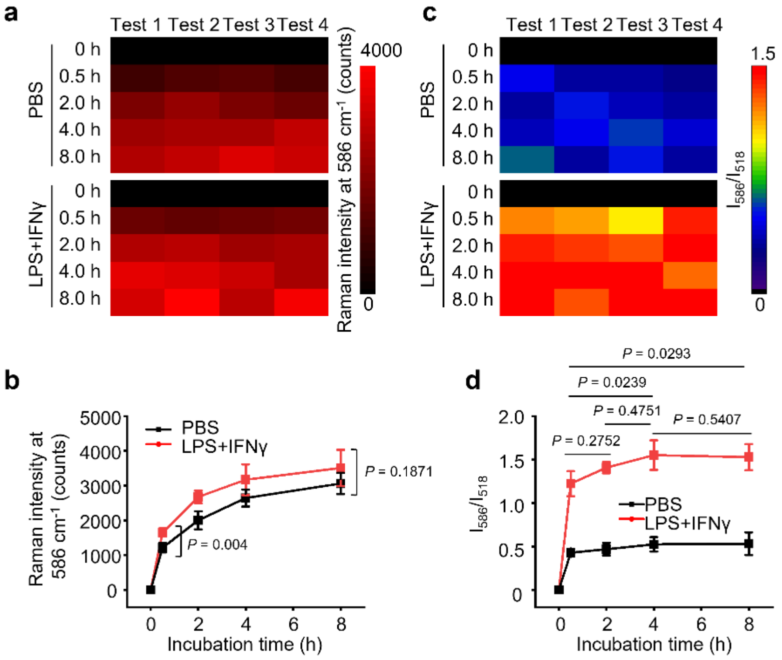

Supplementary figure 26 | Dynamic cellular uptakes of ultraHOCls in primary mouse microglia. a,b, Heat map (**a**) and quantification (**b**) of SERS intensities collected at 586 cm^{-1} of PBS-treated and LPS-treated microglia after incubating with ultraHOCls for different times. **c,d,** Heat map (**c**) and quantification (**d**) of SERS intensity ratios (I_{586}/I_{518}) of PBS-treated and LPS-treated microglia after incubating with ultraHOCls for different times. Data are presented as the mean ± s.d. (n = 4). *P* values were analysed by two-tailed unpaired Student's *t*-tests (**b**) or one-way ANOVA with Tukey's post-hoc test (**d**).

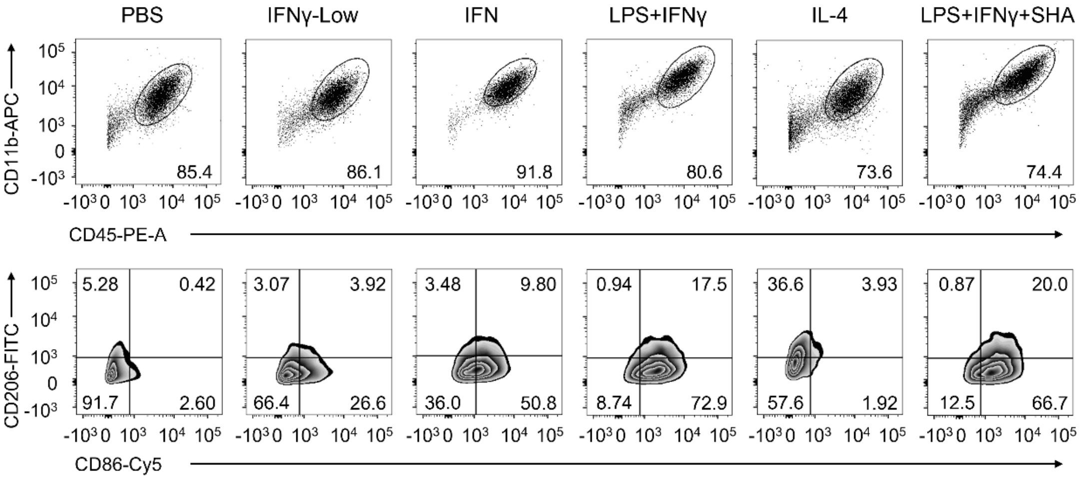

Supplementary figure 27 | Flow cytometry analysis of phenotypic polarization of the cultured primary mouse microglia after various treatments. The primary mouse microglia were stimulated with the following treatments. IFNγ-Low: 40 ng/mL IFNγ; IFNγ: 100 ng/mL IFNγ; LPS+IFNγ: 600 ng/mL LPS plus 100 ng/mL IFNγ; IL-4: 40 ng/mL IL-4; LPS+IFNγ+SHA: 600 ng/mL LPS plus 100 ng/mL IFNγ followed with SHA (500 μM).

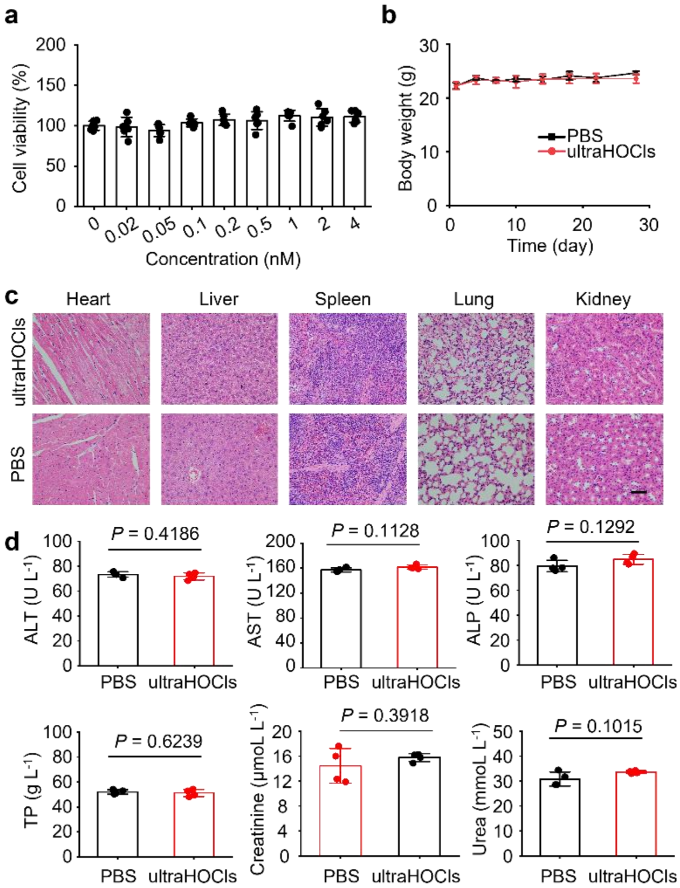

Supplementary figure 28 | Biosafety evaluation of ultraHOCls. **a,** Viabilities of primary mouse microglia after treatment with various concentrations (from 0 to 4 nM) of ultraHOCls for 24 h. Cell viabilities were determined by the CCK-8 assay. Data are presented as the mean ± s.d. (n = 6 biologically independent experiments). **b,** Changes in the body weights of the mice after intravenous injection of ultraHOCls (800 nmol/kg). The mice treated with isovolumetric PBS were used as controls (n = 4 mice per group). **c,** Representative H&E images of tissues (heart, liver, spleen, lung and kidney) that were harvested from mice 10 days after different treatments. Scale bar, 50 μm. **d,** Hepatic function markers (AST, ALP, ALT, serum TP) and renal function markers (creatinine, urea) were tested, and found to be normal compared with the PBS-treated group after 28 days, indicating no noticeable hepatic and renal dysfunctions induced by the ultraHOCls. Data are presented as the mean ± s.d. (n = 4 mice per group). *P* values were analysed by two-tailed unpaired Student's *t*-tests. AST, aspartate aminotransferase; ALP, alkaline phosphatase; ALT, alanine aminotransferases; TP, total protein.

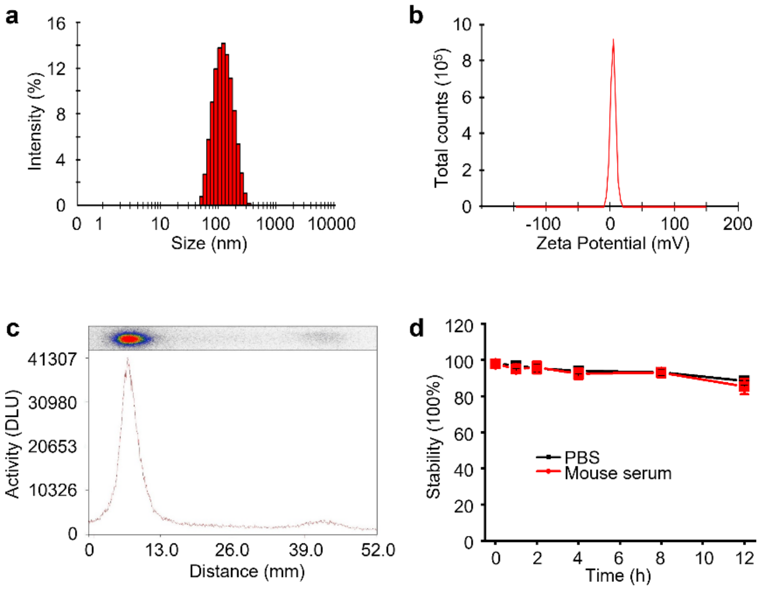

Supplementary figure 29 | Synthesis and characterization of ^{99m}Tc-ultraHOCls. a,b, Dynamic light scattering (**a**) and zeta potential analyses (**b**) showed that ^{99m}Tc-ultraHOCls had similar hydrodynamic diameter and surface potential to ultraHOCls. **c,** The radiochemical purity of ^{99m}Tc-ultraHOCls was greater than 97% as measured by paper chromatography with normal saline as the mobile phase. **d,** Radiostability of ^{99m}Tc-ultraHOCls in PBS (pH 7.4) and mouse serum. Data are presented as the mean ± s.d. (n = 3).

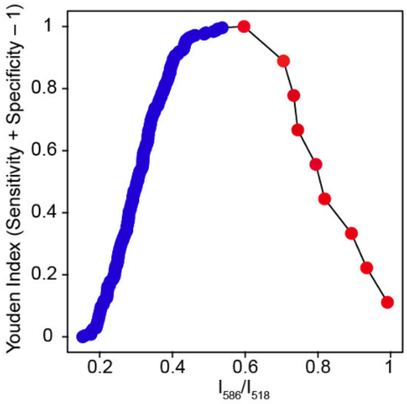

Supplementary figure 30 | Youden's-Index performance for different cut-off values of I_{586}/I_{518}. The best cut-off point of I_{586}/I_{518} is 0.6.

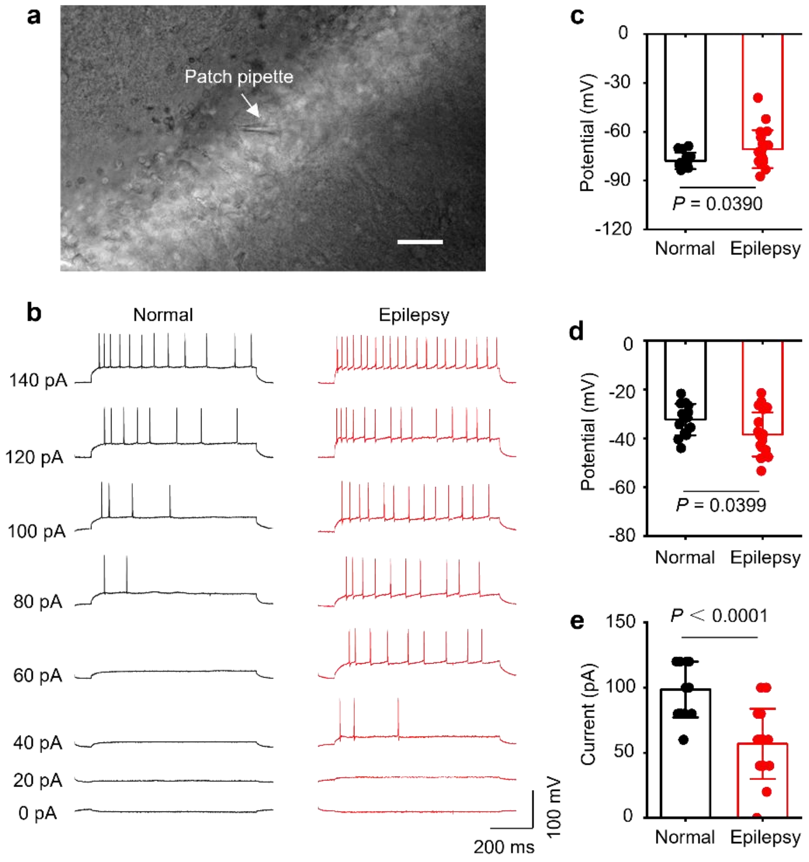

Supplementary figure 31 | Increased excitability of neurons is recorded from resected mouse brain tissues with high I_{586}/I_{518} ratios. a, A bright-field image of a patch pipette attached to the membrane of a hippocampal neuron in resected mouse brain slices derived from a KA model. **b,** Action potential (AP) trains induced by injecting increased currents (0-pA−140-pA with an increment of 20 pA). **c−e,** Statistical analysis of resting membrane potential (**c**), AP threshold (**d**) and rheobase (**e**) recorded from mouse brain slices (n = 14 for normal, n = 19 for epilepsy). Data are presented as the mean ± s.d. *P* values were calculated using unpaired two-tailed Student’s *t*-tests.

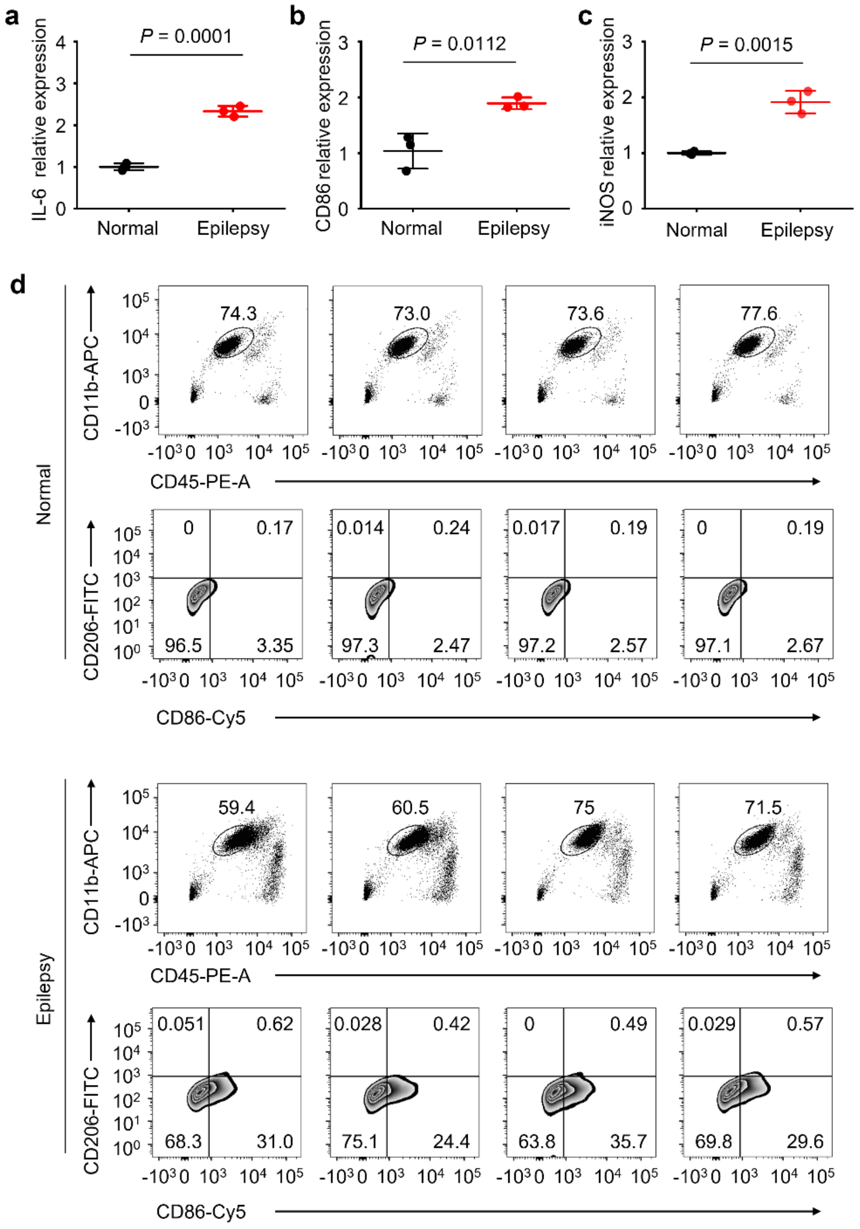

Supplementary figure 32 | Proinflammatory microglia are evident in epileptic foci (EF) of KA models. a–c, Relative mRNA expression of IL-6 (**a**), CD86 (**b**), iNOS (**c**) in resected mouse brain tissues from KA models. **d,** Flow cytometry results of phenotypic polarization of the microglia in resected mouse brain tissues from KA models. All values are presented as the mean ± s.d of biologically independent samples with n = 3 (**a–c**) and n = 4 (**d**). *P* values were calculated using unpaired two-tailed Student's *t*-tests.

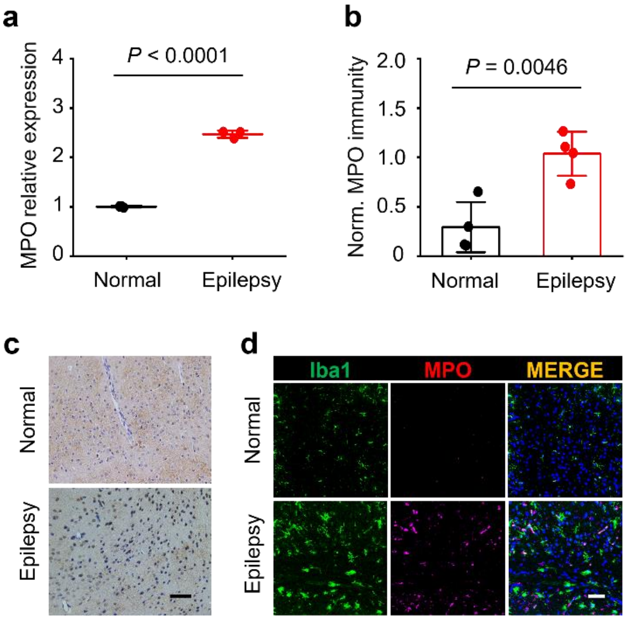

Supplementary figure 33 | Upregulation of MPO is found in the resected mouse brain tissues with higher I_{586}/I_{518} ratios. a, Relative mRNA expression of MPO in resected mouse brain tissues from KA models. **b,** Quantification of the immunoblots results of MPO expression in KA models. **c,** Representative immunohistochemistry of MPO in KA models. Upregulation of MPO was found in epileptic tissues. Scale bar, 50 μm. **d,** Co-localization and quantification of MPO with Iba1 in KA models. Scale bar, 50 μm. All values are presented as the mean ± s.d of biologically independent samples with n = 3 (**a**) and n = 4 (**b**). *P* values were calculated using unpaired two-tailed Student's *t*-tests.

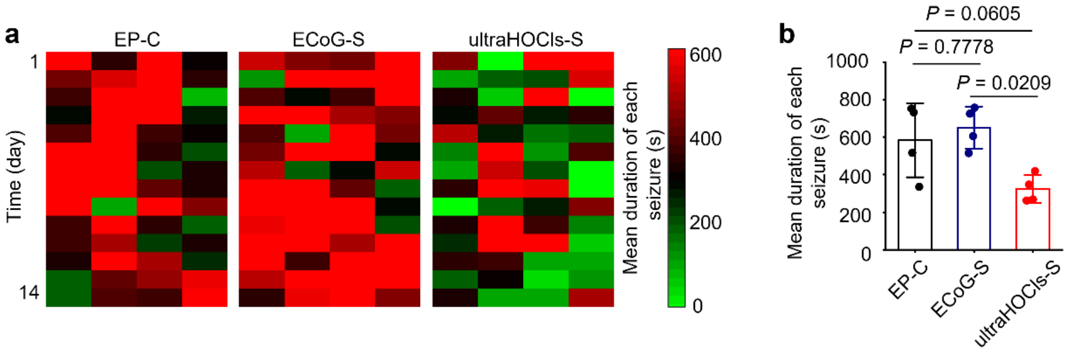

Supplementary figure 34 | UltraHOCls-guided surgery alleviates neuronal seizure activity in KA-induced mouse model. a,b, Heat map (**a**) and quantification (**b**) of mean duration of paroxysmal discharges over time (per 8 h) per mouse in the EP-C, ECoG-S, and ultraHOCls-S groups (n = 4 mice per group). Data are presented as the mean ± s.d. *P* values were analysed by one-way ANOVA with Tukey's post-hoc test.

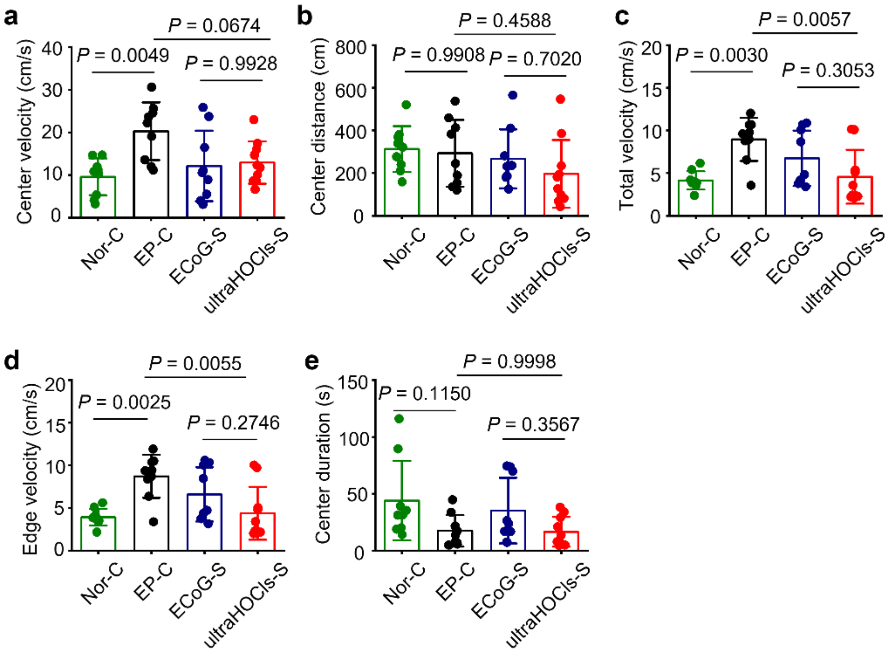

Supplementary figure 35 | Decreased hyperactivity but no obvious reductions in anxiety-like behavior in the open field test in the ultraHOCIs-S group. a−e, The center velocity (**a**), distance traveled in the center (**b**), total velocity (**c**), velocity in the edge (**d**) and duration in the center (**e**) of the open field over the 10-min test period (n = 9 mice per group for the Nor-C, EP-C, ECoG-S groups, n = 10 mice for the ultraHOCIs-S group). Data are presented as the mean ± s.d. *P* values were analysed by one-way ANOVA with Tukey's post-hoc test.

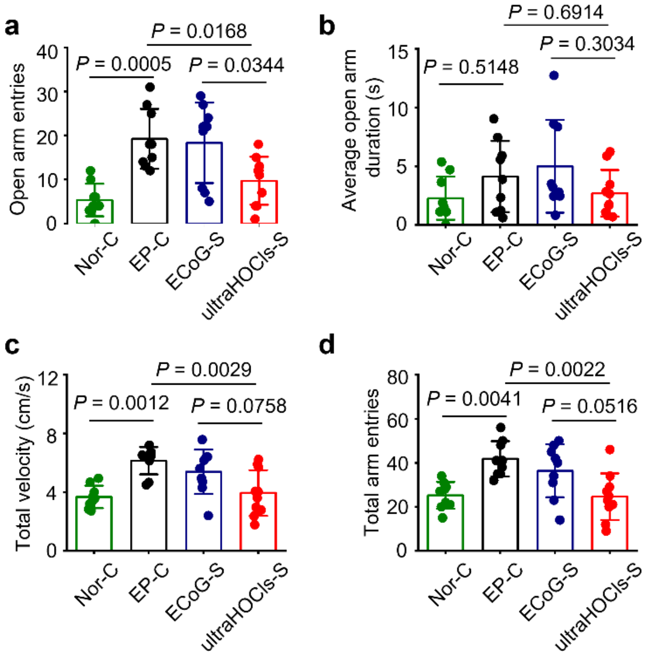

Supplementary figure 36 | Decreased hyperactivity but no obvious reductions in anxiety-like behavior in the elevated plus-maze test in the ultraHOCls-S group. a–d, The entries in the open arms (**a**), the average duration in the open arms (**b**), total velocity (**c**), and the number of total arm entries (**d**) over the 5-min test period (n = 9 mice per group for the Nor-C, EP-C, ECoG-S groups, n = 10 mice for the ultraHOCls-S group). Data are presented as the mean ± s.d. *P* values were analysed by one-way ANOVA with Tukey's post-hoc test.

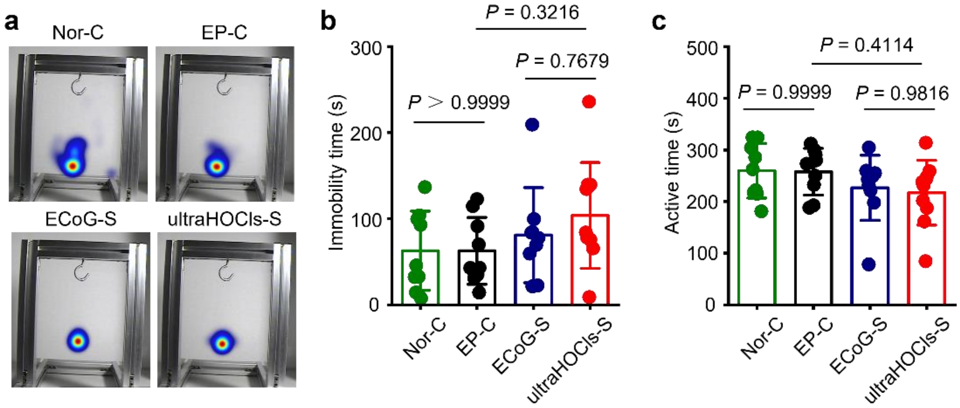

Supplementary figure 37 | No obvious depression-related behavior alteration is observed in the tail suspension test in the ultraHOCls-S group. a, Representative heatmaps show traveling trace. **b,c,** Immobility time (**b**) and active time (**c**) in the tail suspension test (n = 9 mice per group for the Nor-C, EP-C, ECoG-S groups, n = 10 mice for the ultraHOCls-S group). Data are presented as the mean ± s.d. *P* values were analysed by one-way ANOVA with Tukey's post-hoc test.

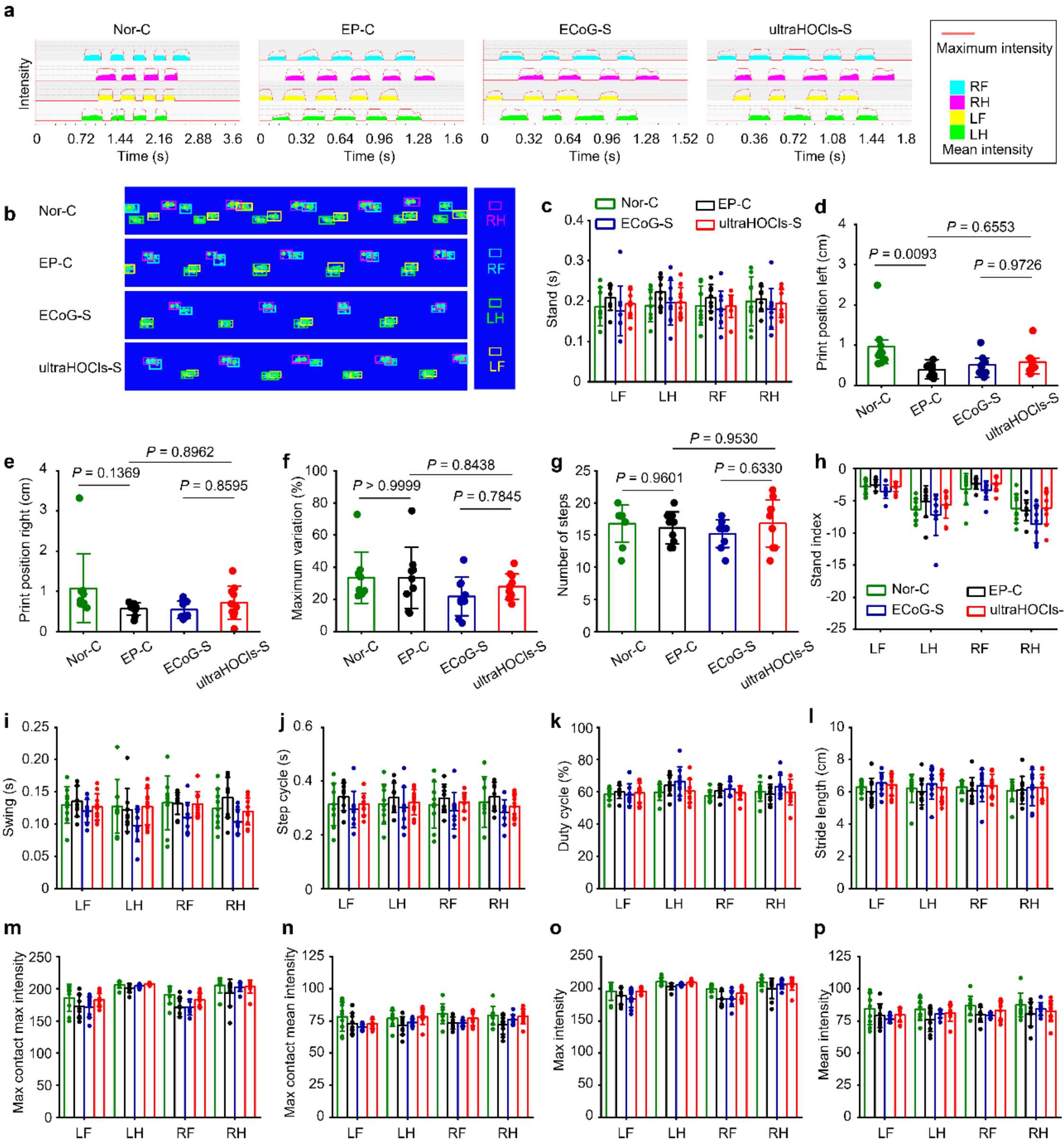

Supplementary figure 38 | No deficits in motor function and coordination were observed in the Catwalk gait analysis in the ultraHOCls-S group. a, 2D footprint intensity images of the legs in the various experimental groups. The time course of the weight load was measured as mean intensity. **b,** Representative gait images in the Catwalk gait analysis. **c−p,** Quantification of dynamic paw parameters included stand (**c**), the print position of left (**d**), the print position of right (**e**), the percentage of maximum variation (**f**), number of steps (**g**), stand index of four paws (**h**), swing of four paws (**i**), step cycle of four paws (**j**), the percentage of duty cycle of four paws (**k**), stride length of four paws (**l**), max contact max intensity (**m**), max contact mean intensity (**n**), max intensity (**o**), and mean intensity (**p**). RF, right front paw; RH, right hind paw; LF, left front paw; LH, left hind paw (n = 9 mice per group for the Nor-C, EP-C, ECoG-S groups, n = 10 mice for the ultraHOCls-S group). Data are presented as the mean ± s.d. *P* values were analysed by one-way ANOVA with Tukey's post-hoc test.

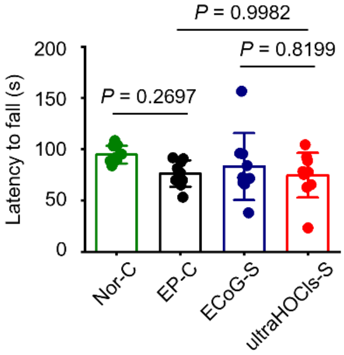

Supplementary figure 39 | No deficits in motor coordination are observed in the accelerating rotarod test in the ultraHOCls-S group. The time of latency to fall in the accelerating rotarod test (n = 9 mice per group for the Nor-C, EP-C, ECoG-S groups, n = 10 mice for the ultraHOCls-S group). Data are presented as the mean ± s.d. *P* values were analysed by one-way ANOVA with Tukey's post-hoc test.

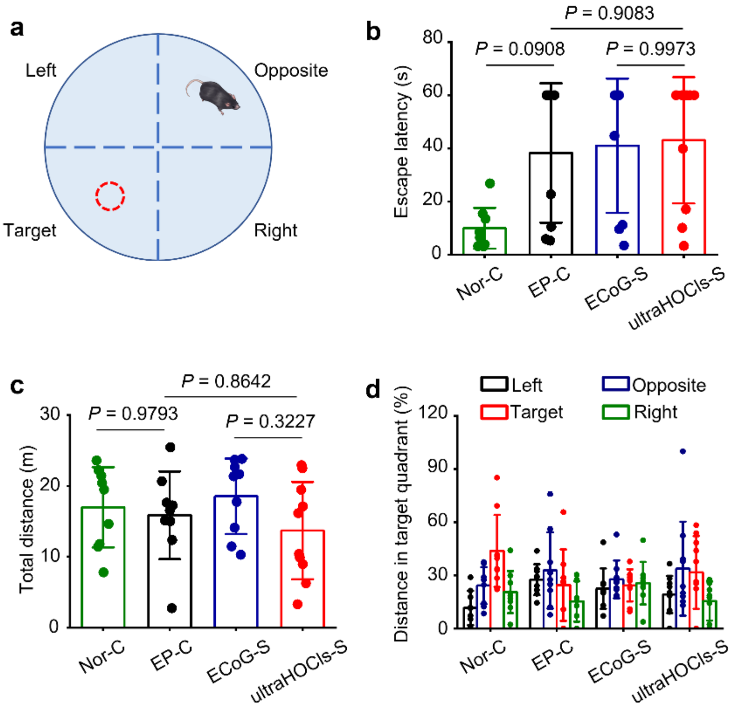

Supplementary figure 40 | UltraHOCls-guided surgery does not aggravate the spatial memory damage. a, Scheme of the Morris water maze. **b,c,** Mean latency of escape (**b**) and total distance (**c**) from the Morris Water Maze test. **d,** The percentage of distance traveled in four quadrants (n = 9 mice per group for the Nor-C, EP-C, ECoG-S groups, n = 10 mice for the ultraHOCls-S group). Data are presented as the mean ± s.d. *P* values were analysed by one-way ANOVA with Tukey's post-hoc test.

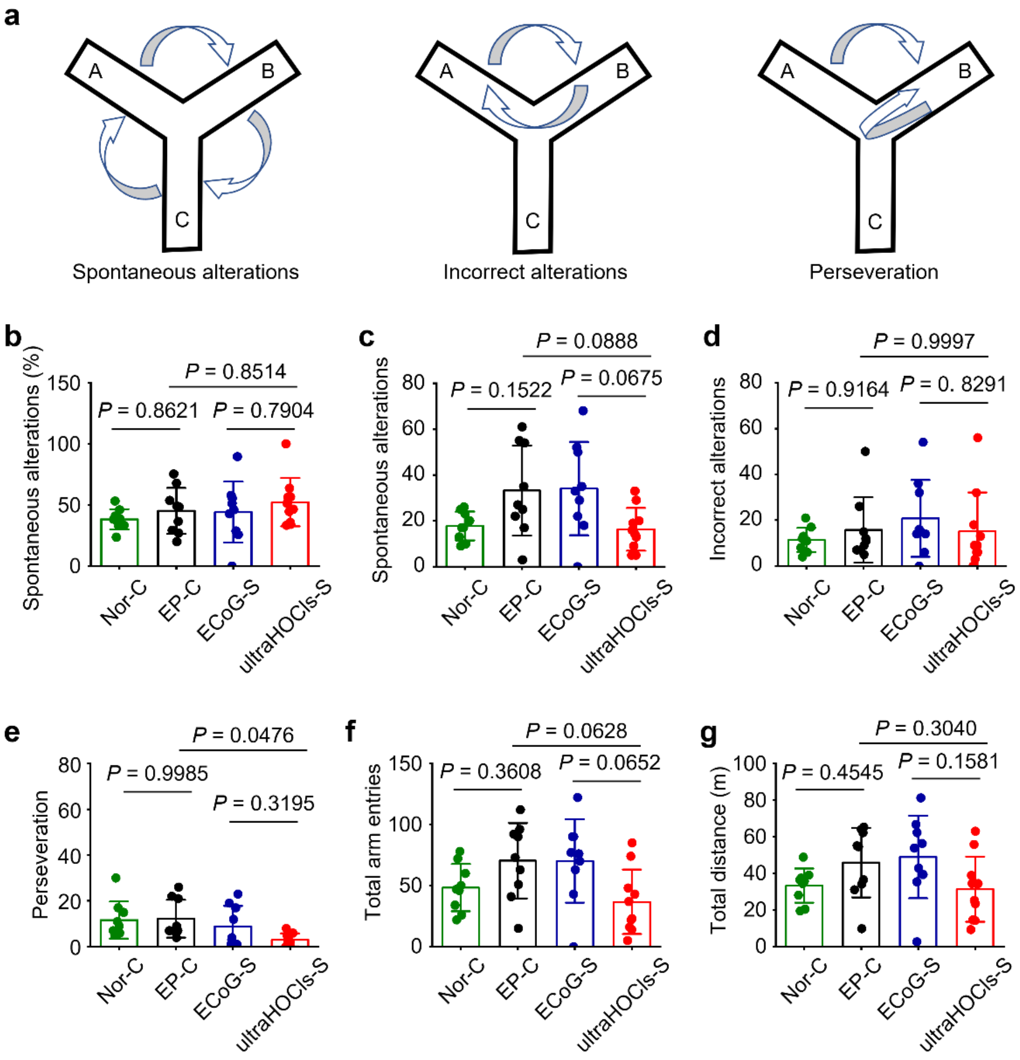

Supplementary figure 41 | No obvious prefrontal cortex-dependent cognitive impairment in the Y-maze test after treatment of ultraHOCls-guided surgery. a, Schematic illustration of the spontaneous alternation (correct alternation), incorrect alternation and perseveration in the Y-maze test. **b−g,** Quantification of the percentage of spontaneous alternation (**b**), spontaneous alternation (**c**), the number of incorrect alternations (**d**), the number of perseveration (**e**), the total number of arm entries (**f**), and total distance (**g**) in the 5-min Y-maze test (n = 9 mice per group for the Nor-C, EP-C, ECoG-S groups, n = 10 mice for the ultraHOCls-S group). Data are presented as the mean ± s.d. *P* values were analysed by one-way ANOVA with Tukey's post-hoc test.

Supplementary Table 1 Baseline characteristics of patients with intractable epilepsy involved in the study. Clinical and neuropathological information includes Age, age at surgery (years); Duration, epilepsy history duration (years); Gender of the patients; Location, Location of resected tissues; Histology and antiseizure drugs used of the patients. FCD IIa, Focal cortical dysplasia type IIa.

Patient	Age	Duration	Gender	Location	Histology
1	22	6	M	Right occipital lobe	FCD IIa
2	30	10	F	Occipital-temporal junction of the left hemisphere	–
3	57	5	F	Right frontal lobe	Neuron loss; Gliosis
4	36	36	M	Left temporal lobe	FCD IIa
5	25	10	M	Left hippocampus	Hippocampal sclerosis
6	36	8	M	Left temporal lobe	Cystic degeneration and glial scar formation
7	40	10	F	Right hippocampus	Hippocampal sclerosis
8	17	8	M	Right temporal lobe	Neuron disorganization; Gliosis.
9	39	6	M	Left temporal lobe	Neuron disorganization
10	51	30	F	Right temporal lobe	neuron loss; Nuclear pyknosis; Gliosis.
11	23	18	M	Right hippocampus	Hippocampal sclerosis
12	20	8	F	Right temporal lobe	FCD IIa

Supplementary Table 2 Baseline characteristics of control patients without a history of seizures involved in the study. Clinical and neuropathological information including: Age, age at surgery (years); Gender of the patients; Location, Location of resected tissues; Histology of the patients.

Patient	Age	Gender	Location	Histology
1	49	M	Bilateral frontal lobes	Glioblastoma (WHO IV)
2	20	M	Right side of the hypothalamus	Glioblastoma (WHO IV)
3	47	M	Left thalamus	Glioblastoma (WHO IV)
4	59	F	Right forehead and temporal lobe	Glioblastoma (WHO IV)
5	24	F	Cerebellar vermis	Pilocytic astrocytoma (WHO I)
6	46	F	Right cingulate gyrus	Glioblastoma (WHO IV)
7	22	F	Lateral ventricle	Central neurocytoma (WHO II)
8	27	F	Right temporal lobe	Cavernous hemangioma
9	55	M	Right temporal lobe	Old hemorrhage with gliosis
10	36	F	Brainstem	Cavernous hemangioma
11	32	F	Left temporal lobe	Arteriovenous malformation
12	16	M	Left occipital lobe	Arteriovenous malformation

Supplementary Table 3 Sequences of primers used in RT-PCR experiments.

Gene name	Forward primer (5’−3’)	Reversed primer (5’−3’)
For human		
GAPDH	GTCTCCTCTGACTTCAACAGCG	ACCACCCTGTTGCTGTAGCCAA
MPO	CCCATGGAACTCCTATCCTA	CTAGGAGGAGTCACTAGTGG
CD86	CCATCAGCTTGTCTGTTTCATTCC	GCTGTAATCCAAGGAATGTGGTC
iNOS	AGTCGAAAACTGAGGCTCCG	TGCCTTGAGAACTTCGGGAC
IL-6	TTCGGTCCAGTTGCCTTCTC	CACCTCCTTTCTCAGGGCTG
CD206	TTAAGGGGGATCTGGGGAGG	CCATTCGCTCCCAAGTCAGT
Arg-1	CTTGATTGGGGAGAGGCAGG	AACAGAAGACTTGCCCTGGG
TGF-β	TACCTGAACCCGTGTTGCTCTC	GTTGCTGAGGTATCGCCAGGAA
For mouse		
GAPDH	AGGTCGGTGTGAACGGATTTG	TGTAGACCATGTAGTTGAGGTCA
MPO	CGTGTCAAGTGGCTGTGCCTAT	AACCAGCGTACAAAGGCACGGT
CD86	TGTTTCCGTGGAGACGCAAG	TTGAGCCTTTGTAAATGGGCA
IL-6	TAGTCCTTCCTACCCCAATTTCC	TTGGTCCTTAGCCACTCCTTC
iNOS	GTTCTCAGCCCAACAATACAAGA	GTGGACGGGTCGATGTCAC
CD206	CTCTGTTCAGCTATTGGACGC	CGGAATTTCTGGGATTCAGCTTC
Arg-1	CTCCAAGCCAAAGTCCTTAGAG	AGGAGCTGTCATTAGGGACATC
TGF-β	CTCCCGTGGCTTCTAGTGC	GCCTTAGTTTGGACAGGATCTG

Supplementary Table 4 Antibodies used for immunofluorescence studies, flow cytometric assays and immunoblotting studies in the study.

Antibodies	Source	Identifier
Immunofluorescence antibodies		
Goat ionised calcium-binding adaptor molecule 1 (Iba1) polyclonal antibody	Novus Biologicals	Cat# NB100-1028 RRID: AB_521594
Recombinant anti-myeloperoxidase antibody	Abcam	Cat# ab208670 RRID: AB_2864724
Recombinant anti-CD163 antibody	Abcam	Cat# ab182422 RRID: AB_2753196
Recombinant anti-iNOS antibody	Abcam	Cat# ab178945 RRID: AB_2861417
Flow cytometric antibodies		
PE anti-human CD45 antibody	Biolegend	Cat# 368510 RRID: AB_2566370
APC anti-human CD11b antibody	Biolegend	Cat# 301309 RRID: AB_314161
FITC anti-human CD206 antibody	Biolegend	Cat# 321103 RRID: AB_571904
PerCP/Cyanine5.5 anti-human CD86 antibody	Biolegend	Cat# 305419 RRID: AB_1575070
PE/Cyanine7 anti-mouse CD45 antibody	Biolegend	Cat# 103114 RRID: AB_312979
PerCP/Cyanine5.5 anti-mouse/human CD11b antibody	Biolegend	Cat# 101227 RRID: AB_2565948
Alexa Fluor® 488 anti-mouse CD206 antibody antibody	Biolegend	Cat# 141710 RRID: AB_893232
PE anti-mouse CD86	Biolegend	Cat# 105007 RRID: AB_313150
Immunoblotting antibodies		
Recombinant anti-myeloperoxidase antibody	Abcam	Cat# ab208670 RRID: AB_2864724
Anti-GAPDH antibody-loading control	Abcam	Cat# ab70699 RRID: AB_1209569

Supplementary Table 5 Definition of gait parameters involved in Catwalk gait analysis.

Parameters	Definition
Print position	The distance between the position of the hind paw and the previously placed front paw on the ipsilateral side.
Cadence	Step numbers per second.
Print area	Total surface area of a print.
Stand	The duration that a paw in contact with glass plate.
Maximum variation	The maximum variation in running speed.
Number of steps	Total step numbers during a run.
Stand index	The parameter for describing the speed at which the paw loses contact with the glass plate.
Swing	The duration that a paw does not in contact with glass plate.
Step cycle	The sum duration of Stand and Swing.
Duty cycle	The percentage of Stand in Step Cycle.
Stride length	The distance between successive positions of the same claw.
Max intensity	The maximum intensity of the complete paw.
Mean intensity	The mean intensity of the complete paw.
Max contact max intensity	The maximum intensity of a paw when it achieves maximum contact with the glass plate.
Max contact mean intensity	The mean intensity of a paw when it achieves maximum contact with the glass plate.

References

1. Zhang, Y. et al. Noninvasively Imaging Subcutaneous Tumor Xenograft by a Handheld Raman Detector, with the Assistance of an Optical Clearing Agent. *ACS Applied Materials & Interfaces* **9**, 17769−17776 (2017).
2. Gao, X. et al. Guiding brain-tumor surgery via blood-brain-barrier-permeable gold nanoprobes with acid-triggered MRI/SERRS signals. *Advanced Materials* **29**, 1603917 (2017).
3. Wang, C. et al. An electric-field-responsive paramagnetic contrast agent enhances the visualization of epileptic foci in mouse models of drug-resistant epilepsy. *Nature Biomedical Engineering* **5**, 278−289 (2021).